Icarus 205 (2010) 165–182

Contents lists available at ScienceDirect

Icarus

journal homepage: www.elsevier.com/locate/icarus

Aeolian bedforms, yardangs, and indurated surfaces in the Tharsis Montes as seen by the HiRISE Camera: Evidence for dust aggregates

N.T. Bridges [a,*], M.E. Banks [b], R.A. Beyer [c], F.C. Chuang [d], E.Z. Noe Dobrea [a], K.E. Herkenhoff [e], L.P. Keszthelyi [e], K.E. Fishbaugh [f], A.S. McEwen [b], T.I. Michaels [g], B.J. Thomson [h], J.J. Wray [i]

[a] Jet Propulsion Laboratory, California Institute of Technology, Pasadena, CA 91109, USA
[b] Lunar and Planetary Laboratory, University of Arizona, Tucson, AZ 85721-0092, USA
[c] SETI Institute, Mountain View, CA 94043, USA
[d] Planetary Science Institute, Tucson, AZ 85719, USA
[e] U.S. Geological Survey, Flagstaff, AZ 86001, USA
[f] Center for Earth and Planetary Studies, Smithsonian Air and Space Museum, Washington, DC 20013-7012, USA
[g] Southwest Research Institute, Boulder, CO 80302-5142, USA
[h] The Johns Hopkins University, Applied Physics Laboratory, Laurel, MD 20723, USA
[i] Department of Astronomy, Cornell University, Ithaca, NY 14853, USA

ARTICLE INFO

Article history:
Received 5 November 2008
Revised 22 April 2009
Accepted 22 May 2009
Available online 2 June 2009

Keywords:
Mars
Mars, Surface

ABSTRACT

HiRISE images of Mars with ground sampling down to 25 cm/pixel show that the dust-rich mantle covering the surfaces of the Tharsis Montes is organized into ridges whose form and distribution are consistent with formation by aeolian saltation. Other dusty areas near the volcanoes and elsewhere on the planet exhibit a similar morphology. The material composing these "reticulate" bedforms is constrained by their remote sensing properties and the threshold curve combined with the saltation/suspension boundary, both of which vary as a function of elevation (atmospheric pressure), particle size, and particle composition. Considering all of these factors, dust aggregates are the most likely material composing these bedforms. We propose that airfall dust on and near the volcanoes aggregates *in situ* over time, maybe due to electrostatic charging followed by cementation by salts. The aggregates eventually reach a particle size at which saltation is possible. Aggregates on the flanks are transported downslope by katabatic winds and form linear and "accordion" morphologies. Materials within the calderas and other depressions remain trapped and are subjected to multidirectional winds, forming an interlinked "honeycomb" texture. In many places on and near the volcanoes, light-toned, low thermal inertia yardangs and indurated surfaces are present. These may represent "duststone" formed when aggregates reach a particle size below the threshold curve, such that they become stabilized and subsequently undergo cementation.

1. Background

Aeolian processes and landforms on Mars, combined with Earth analog comparisons, has been a fertile area of study for decades (e.g., Greeley and Iversen, 1985; Greeley et al., 1992, 2002; Sullivan et al., 2008). This research, combined with wind tunnel studies, and *in situ* observations from the Mars Exploration Rovers (MER), indicates that martian dunes and ripples are composed of sand. At the MER *Spirit* site, ordinary ripples are composed of fine sand (predominated by <100 μm sizes), with "coarse-grained" ripples consisting of a carapace of coarse sand (700–1800 μm) overlying fine sand (Sullivan et al., 2008). Dunes have not been studied *in situ*, but probably consist of fine sand. Near-surface winds transport the grains and organize them into bedforms, through either saltation (fine sand) or creep (coarse sand and granules). With the advent of high resolution (down to 25 cm/pixel ground sampling distance) and high SNR (>100:1) images from the High Resolution Imaging Science Experiment (HiRISE) on the Mars Reconnaissance Orbiter (MRO) (McEwen et al., 2007), new details of these features are evident. Recent discoveries include superposed bedforms on dunes and ripples indicative of modification from multiple wind regimes and small bedforms within fresh craters and gullies (Bridges et al., 2007).

Dust, with typical suspended sizes of 1–2 μm, is at the small end of the particle size spectrum. It is abundant on Mars, with local and global dust storms observable from orbiters and even Earth-based telescopes. Dust can remain suspended in the atmosphere

* Corresponding author. Address: Jet Propulsion Laboratory, California Institute of Technology, MS 183-501, 4800 Oak Grove Dr., Pasadena, CA 91109, USA. Fax: +1 818 393 5059.
E-mail address: nathan.bridges@jpl.nasa.gov (N.T. Bridges).

0019-1035/$ - see front matter © 2009 Elsevier Inc. All rights reserved.
doi:10.1016/j.icarus.2009.05.017

for long periods, especially under turbulent conditions, slowly falling to the surface in quiescent times. As such, dust is not expected to participate in near-surface aeolian processes that form ripples and dunes. With the advent of orbital albedo and thermal measurements in the 1970s, high surface dust concentrations were found in certain regions of the planet (e.g., Zimbelman and Kieffer, 1979; Christensen, 1986). The dustiest areas correspond to the classic bright terrains of Tharsis, Elysium, and Arabia, with predicted dust thicknesses of 0.1–2 m (Christensen, 1986). The first two provinces contain shield volcanoes that show classic volcanic features at scales down to 10 s of meters per pixel.

The prevailing view is that dust settles from the martian atmosphere at rates of a few to almost 50 μm per year. It becomes trapped on the volcanoes because surface friction speeds sufficient to liberate it from the surface are rarely obtained under the low local pressures (down to 0.5 mb) (Christensen, 1988). General circulation models (GCMs) indicate that dust deposition is nearly balanced by removal by dust devils (Kahre et al., 2006). Based on thicknesses and rates of deposition, the dust deposits are estimated to have ages of 10^5–10^6 years. However, even at the resolution available from the Viking Orbiters, some local transport is evident. At this scale, darker (albedo 0.2–0.3) collars within brighter annuli circumscribe the upper 10–20 km elevations of the main Tharsis Montes and Elysium Mons (Veverka et al., 1977; Thomas et al., 1981; Lee et al., 1982). The albedo of the collars varies seasonally in conjunction with atmospheric dust loading. The margins of the bright annuli and collars have downslope streaks that are most prominent following the clearing from global dust storms. The

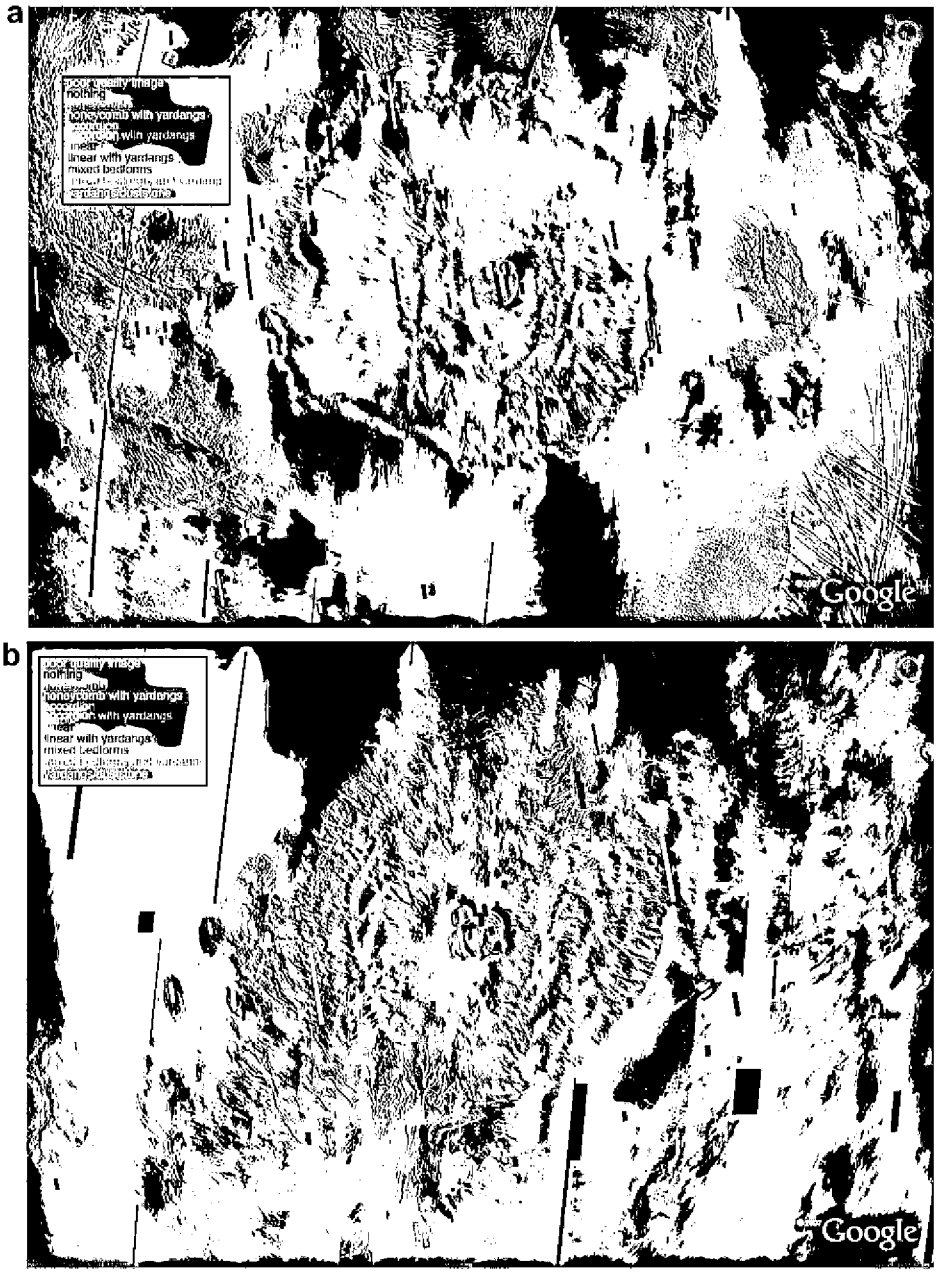

Fig. 1. THEMIS daytime infrared mosaic of the Tharsis Montes and surrounding plains overlaid by the footprints of HiRISE images. Each footprint is color-coded by the dominant type of reticulate bedforms and presence of yardangs in that image. The boxes labeled "nothing" may contain traditional ripples or dunes, but not reticulate bedforms or yardangs. (a) Olympus Mons, (b) Ascraeus Mons, (c) Pavonis Mons, (d) Arsia Mons. (For interpretation of the references to color in this figure legend, the reader is referred to the web version of this paper.)

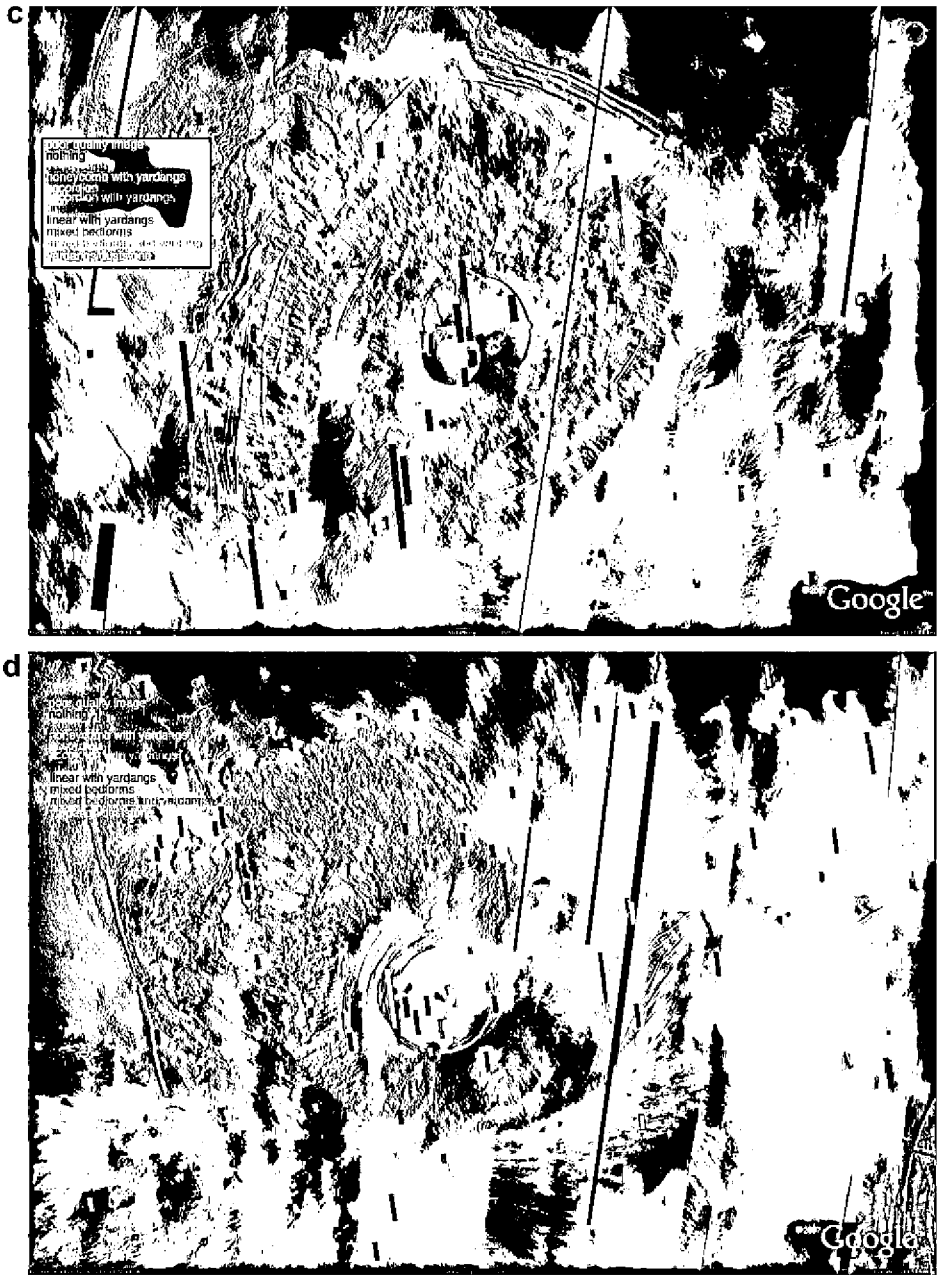

Fig. 1 (*continued*)

brightness contrast between the annuli and collars is also most extreme at this time and then declines thereafter. These observations indicate that at least some dust is deposited on the volcano flanks and liberated by downslope winds. Daytime upslope wind flows and nighttime katabatic near-surface winds at speeds of ~20–100 m s^{-1} on volcanoes are predicted by regional meso-scale atmospheric models (Magalhaes and Gierasch, 1982; Michaels et al., 2006), with deflation estimated at >1 μm year (Kahre et al., 2006). With the advent of the Mars Orbiter Camera (MOC), with a resolution of a few meters, wind tails and aeolian textures radiating down the volcano flanks from the calderas were seen (Malin and Edgett, 2001). In addition, mantled bedforms, at a scale coarser than those reported here, were documented in the high elevation flanks and summit areas of the Tharsis Montes (Edgett and Malin, 2000). This indicates that the katabatic winds not only remove dust, but also modify the surface.

No bedforms were seen on the volcanoes prior to MOC. This is consistent with fundamental aeolian physics, which predict that dust on the volcanoes will either accumulate or go into suspension, depending on the friction speed. The particle size is too small for saltation (see a more detailed discussion in Section 4.2 of this paper). Therefore, it was surprising that HiRISE images of the volcanoes showed an intricate suite of ridges interpreted as bedforms (Bridges et al., 2007), with some features possibly erosional scars in a weakly indurated mantle (Keszthelyi et al., 2008). The integrated, commonly polygonal, reticulate pattern at the meter scale was noted on all the major volcanoes, regardless of elevation (Bridges et al., 2007). The reticulated mantle was measured in two location to have thicknesses of at least 4 m (Keszthelyi et al., 2008) and continued analysis of HiRISE images since this paper are consistent with these observations. It was also observed that some yardangs had a "polygonal" texture similar to the bedforms, leading to speculation that there could be a genetic relationship.

The work of Bridges et al. (2007) was a preliminary report on the general appearance and location of reticulate ridges. Now, almost a year later, with more HiRISE coverage and time to integrate

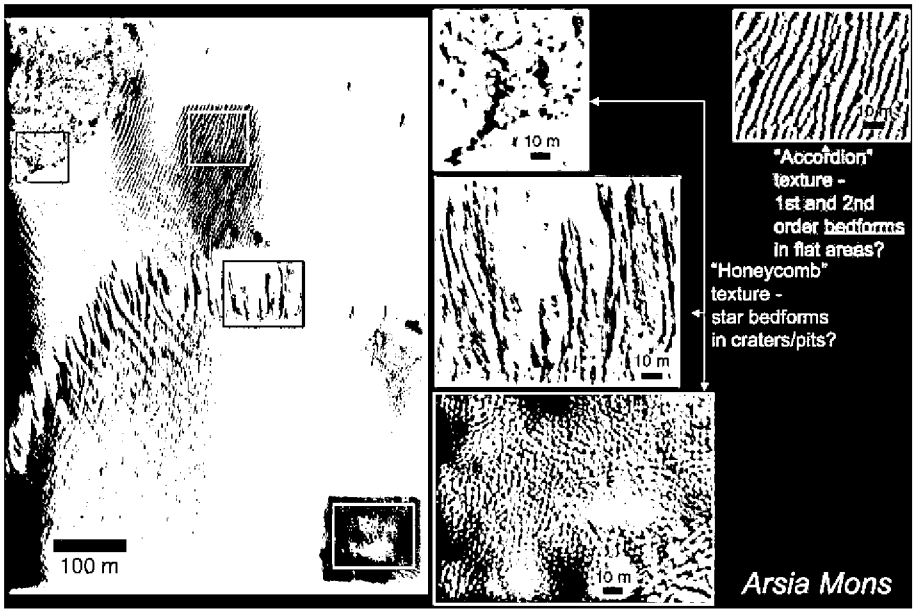

Fig. 2. Portion of HiRISE image PSP_005836_1735 showing pits and adjacent plains on the north flank of Arsia Mons. Note the association of reticulate bedform type with local topography. Colored boxes show location of enlargements to the right. (For interpretation of the references to color in this figure legend, the reader is referred to the web version of this paper.)

other data sets and aeolian physics more completely, we propose a model for the origin, evolution, composition, grain size and possible fate of the reticulate ridges. They and other aeolian features are mapped out on the four major Tharsis Montes. The results lead us to interpret many of these features as saltation bedforms. Aeolian physics and other data are used to constrain the wind regime and physical properties of the constituent particles. We propose that the bedforms are dust aggregates that eventually lithify into abradable yardangs and indurated surfaces, a "duststone" that has no known terrestrial analog.

2. Methods

To qualitatively determine the distribution of reticulate ridges and other features we used a modification of Google Earth whereby various co-registered martian basemaps were overlaid on the terrestrial sphere, effectively producing a virtual Mars, with reprojected map layers, in the Google Earth client (Beyer et al., 2007; Hancher et al., 2008, 2009). The basemaps included Thermal Emission Imaging System (THEMIS) visible and daytime and nighttime infrared mosaics, Mars Orbiter Laser Altimeter (MOLA) topography, and Thermal Emission Spectrometer (TES) thermal inertia, and albedo. Keyhole Markup Language files containing the corner coordinates of HiRISE and other released image products were used to locate the position of the footprints on the basemaps. Using this method, it was possible to systematically examine all images and produce a regional map of the results.

A total of 367 HiRISE images of the Tharsis Montes and nearby plains were examined and then color-coded based on ridge texture, presence of yardangs, lack of any reticulate ridges or yardangs, or unusable because of haze (Fig. 1). Areas examined included the complete caldera, flanks, and plains surrounding the volcanic bases. Where ridges and yardangs occurred together, textural similarities and differences were noted. The distribution and characteristics of reticulate ridges on the four Tharsis Montes were compared to each other to see if there were clear trends. For example, as will be shown, the calderas contain almost exclusively honeycomb ridges whereas linear and accordion ridges and yardangs are located on the flanks.

Gridded TES bolometric thermal inertia (Putzig and Mellon, 2007a) and albedo (Christensen et al., 2001) and MOLA elevation (Smith et al., 2001) of the center point of each HiRISE image were compiled to examine any trends of these parameters with bedform type and presence of yardangs and indurated material. The global distribution of these data, re-sampled to 1/8th degree/pixel, were compared to the HiRISE image center results. These data were incorporated with models of saltation and suspension to constrain the particle size and density of the bedform grains.

3. Results

3.1. Reticulate ridge types and their distribution

Reticulate ridges are distinct from other dunes and ripples on Mars based on their morphology and size, although, as discussed below, they exhibit some common attributes. In the first study of these features with HiRISE (Bridges et al., 2007), the term "reticulate" was applied to a fine polygonal texture, generally consistent with the "honeycomb" morphology described here. We now recognize that reticulate ridges can be categorized into three integrated networks:

(1) Honeycombs are composed of interlocking, azimuthally-symmetric sets of ridges. The spacing of the smallest honeycomb sets is typically a few meters, but there are examples that go down to the limit of resolution (~1 m or less) (Figs. 2 and 3). In some regions, small honeycomb sets are assembled into medium sets whose ridges are ~15–20 m apart (given by red polygons in Fig. 3). Some medium sets are, in turn, enclosed within large sets with ridge spacings of 50–200 m (green outlines in Fig. 3). The honeycomb sets mantle structural, volcanic, and crater topography (e.g., Figs. 2–5) and occur in a diversity of settings. The ridges within the volcano calderas are almost exclusively honeycomb (Figures

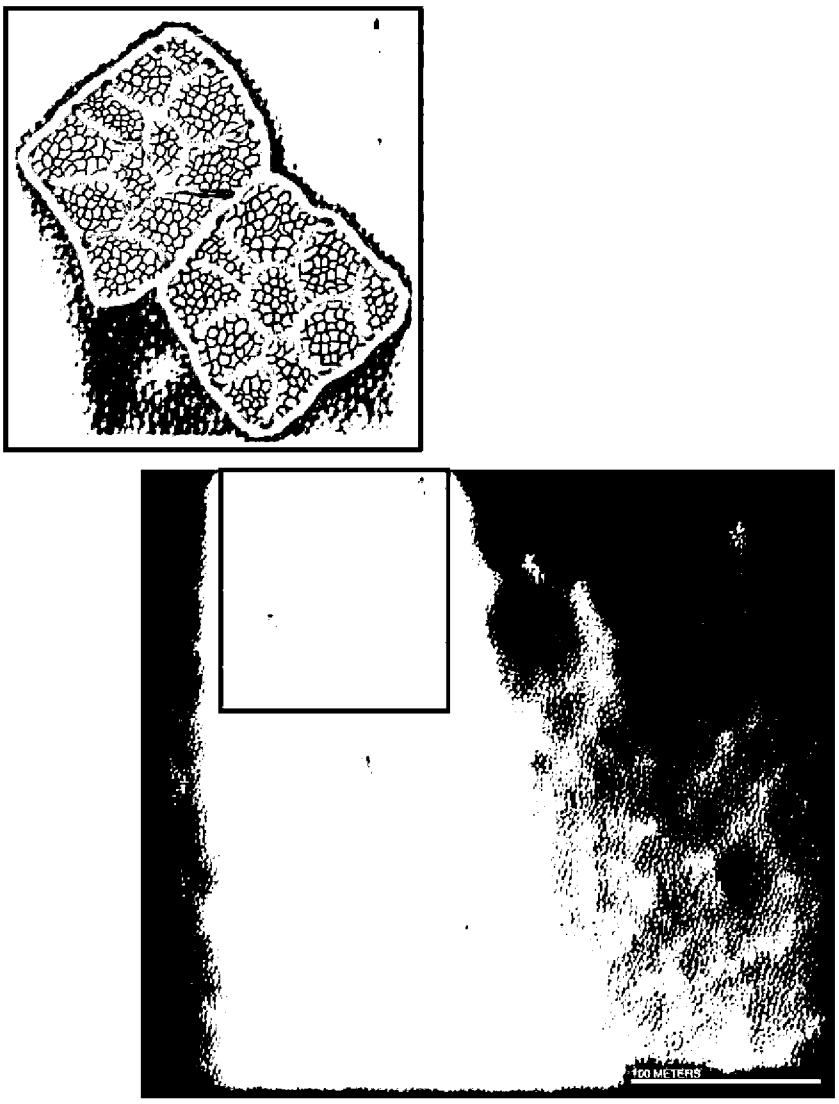

Fig. 3. Example of three scales of honeycomb bedforms. The coarsest (green) scale may be underlying topography that is covered by the reticulate mantle. This image is within the Pavonis Mons caldera (PSP_002249_1805). (For interpretation of the references to color in this figure legend, the reader is referred to the web version of this paper.)

1, 3, and 4), although the limited HiRISE image coverage of the Pavonis Mons caldera shows linear ridges in the north caldera, but honeycomb in the south (Fig. 3). Honeycombs are also found within smaller craters on the volcano flanks. On Olympus Mons, honeycombs are a common morphology on the northwest flank edge (i.e., lower flank), but not along the other flank edges, and are also present on the upper flank southeast of the caldera (Fig. 5). Honeycombs are also common within craters, depressions, and in valleys within the sulci in the surrounding plains. On Ascraeus Mons, they are found on the flanks just south of the caldera and in some plains near the volcanoes, such as southeast of Ascraeus Mons (Fig. 6a and b). There are also honeycombs southeast of Pavonis Mons near small vents (Fig. 7e). The honeycombs, albeit at a finer scale, bear a resemblance to intra-crater dunes that commonly have a morphology analogous to terrestrial star dunes, which are formed from multiple wind regimes. Victoria Crater at the *Opportunity* landing site is a prime example.

(2) Linear ridges exhibit dominant curvilinear ridge sets a few meters apart and up to several kilometers long. They are located on the flanks and lower flank edges of the volcanoes (Fig. 8), with some examples in the surrounding plains. They tend to occur in areas lacking prominent nearby topography and, as such, are rare in calderas or craters. On the volcano flanks, they are oriented perpendicular to the local slope (i.e., circumferential to the caldera).

(3) Accordion ridges contain two linked ridge sets and have attributes of both the linear and honeycomb morphology (Fig. 2). The dominant ridge set has similar spacing and morphometry to the linear ridges and, where found on the volcano flanks, is oriented perpendicular to the local slope. The dominant ridges are bridged by shorter ridges. They are oriented perpendicular to the dominant ridges and so, on the volcano flanks, are parallel to the local slope. The shorter ridges generally define a contiguous line across the larger ridges. Offsets are apparent, but they are the exception rather than the rule. The linear and accordion forms look similar to coarser-scale 1st and *n*th order bedforms seen on dunes and ripples elsewhere on the planet (Bridges et al., 2007). Both the honeycomb and accordion ridges define enclosed basins, with the former nearly equant and the latter elongated parallel to the dominant ridge set.

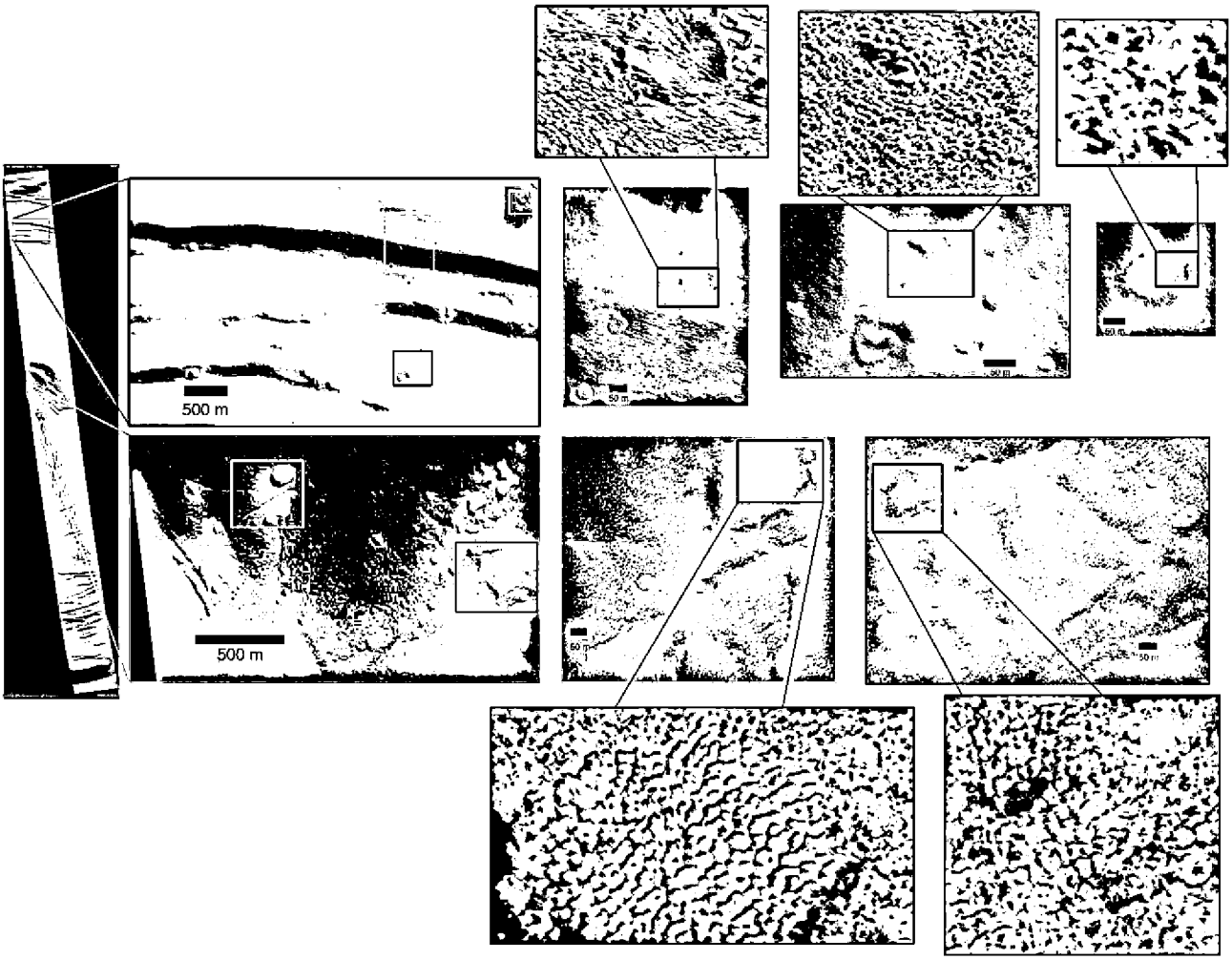

Fig. 4. Honeycomb bedforms within the Olympus Mons caldera. Note that the bedforms superpose underlying structural, volcanic, and crater topography. HiRISE footprint is at left. Colored boxes show location of enlargements to the right. Black boxes within those show outline of stretched enlargements above and below (PSP_004966_1985). (For interpretation of the references to color in this figure legend, the reader is referred to the web version of this paper.)

In many cases, only one type of ridge is prevalent in a HiRISE image. However, there are several examples where two or all three ridge types occur within a span of a few kilometers. There is commonly an association with local topography, in which honeycombs within depressions transition to honeycomb and linear forms on the surrounding plains (e.g., Fig. 2).

In addition to Tharsis, reticulate ridges have been identified in numerous locations across the planet, including Elysium (Bridges et al., 2007; Keszthelyi et al., 2008), draping deposits in Vallis Marineris (Keszthelyi et al., 2008), and in Daedalia Planum (Karunatillake et al., 2009). We have also recently found similar examples in Planum Boreum (Fig. 9a), in some crater wind streaks (Fig. 9b), as bright superposed ridges on the surfaces of dunes in Lyot Crater (Fig. 9c), and on a mound within a crater east of Schiaparelli (Fig. 9d).

3.2. Patterns of reticulate ridge concentration

Reticulate ridges are fairly pervasive in HiRISE images of Tharsis, with some exceptions. They are largely absent on the upper western flank of Olympus Mons and in many of the plains west and northwest of the volcanic scarp (black and green footprints in Fig. 1). In contrast, most of the eastern flank and plains contain these ridges. On the upper flanks of the Montes, reticulate ridges are largely absent at the caldera edge and concentrated on the downslope (away from the caldera) edges of topographic depressions (Fig. 10). An exception is the southern flanks of Ascraeus Mons, which appears covered in honeycombs south of the caldera. The plains west of Ascraeus appear lacking in ridges, although rich in yardangs and indurated surfaces. Several areas of the plains surrounding Arsia Mons lack reticulate ridges, but there is no clear regional trend (Fig. 1d). All images of Pavonis Mons and the nearby plains contain at least some ridges (Fig. 1c).

3.3. Locations of yardangs and wind tails

Reticulate ridges are not the only type of morphology seen on the Tharsis mantle, with yardangs and wind tails also apparent. We identify yardangs as any elevated topography with widths and lengths of 10 s of meters or larger, that also has a high albedo and a scalloped to fluted texture whose long axis is aligned with the long axis of the yardang. In planview, yardangs are non-equant, with many characterized by a blunt edge on one side and a tapered edge on the other, a form that has been attributed to aerodynamic streamlining from upwind and downwind flow, respectively (Greeley and Iversen, 1985). This shape is in marked contrast to bedforms, which consist of distinct ridges of variable form, as described above.

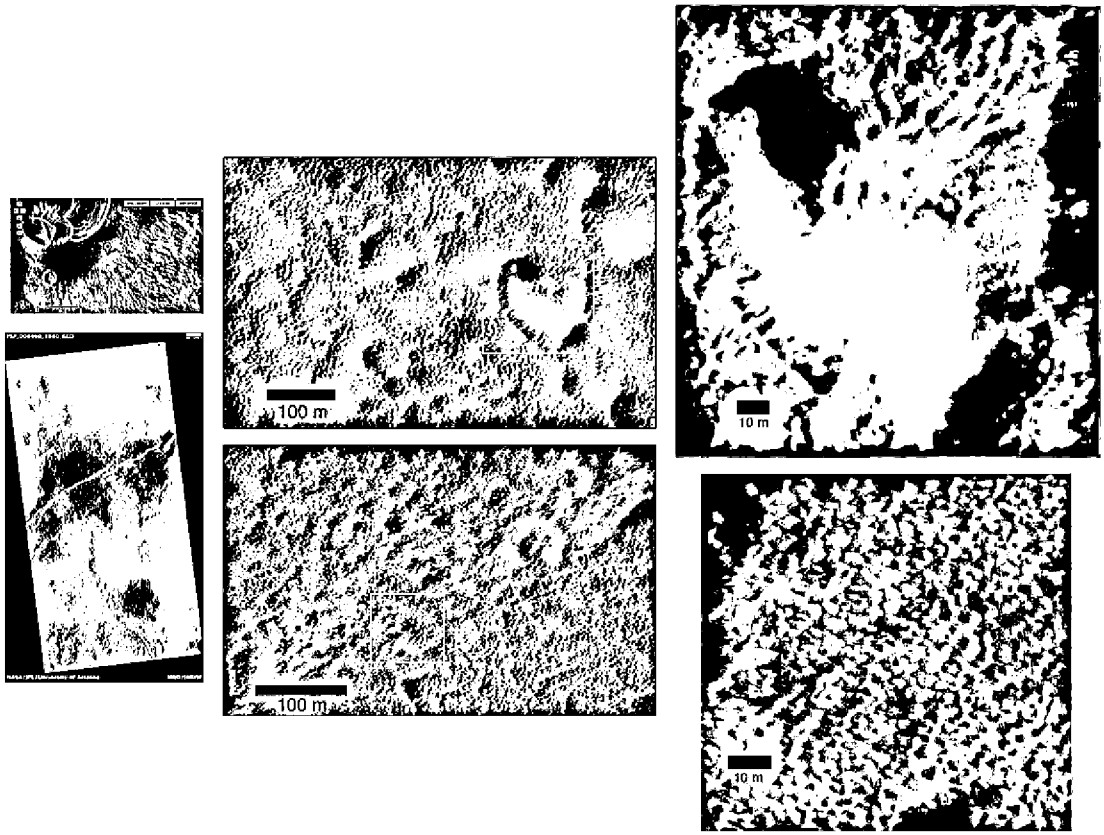

Fig. 5. Example of honeycomb bedforms found on the Olympus Mons flanks. This location is anomalous, as most honeycombs are located within the caldera and depressions. Colored boxes show location of enlargements to the right. The upper left frame shows the image location, the lower right is the complete HiRISE images. Colored boxes show outline of enlargements at right (PSP_*008460_1980*). (For interpretation of the references to color in this figure legend, the reader is referred to the web version of this paper.)

Yardangs are common along the mid to lower flanks of the Tharsis Montes (Figs. 1 and 11). Some are also found on the nearby plains. Wind tails are commonly associated with flank yardangs. On the flanks, yardang tapered edges and wind tails point radially away from the calderas. In some cases, it is difficult to determine if point-shaped features downslope of blunt edges represent wind tails or are the downwind portion of yardangs (Fig. 11).

3.4. Other correlations

3.4.1. Elevation

Reticulate ridges in Tharsis are found at elevations from −2 to >23 km (Fig. 12c). There is no clear association between distribution or morphology and elevation. For example, honeycomb ridges at the highest elevations on the Tharsis Montes look similar to those on the plains.

3.4.2. Albedo and thermal inertia

Reticulate ridges occur exclusively in areas of high albedo and low thermal inertia, regardless of elevation (Fig. 12). Albedo and inertia values range from 0.24 to 0.32 and 10 to 666 J m^{-2} K^{-1} $s^{-0.5}$, respectively. These areas are generally coincident with a high dust cover index (Ruff and Christensen, 2002). The range of albedo and thermal inertia compares to a planet-wide distribution of 0.06–0.32 and <24 to >2000 J m^{-2} K^{-1} $s^{-0.5}$, respectively (Fig. 12b). More than 85% of the imaged locations with reticulate bedforms and yardangs have albedos greater than 0.27 and thermal inertias less than 200 J m^{-2} K^{-1} $s^{-0.5}$ (Fig. 12e and f), making them distinct from the three thermal inertia–albedo units mapped by Mellon et al. (2000). Two of three images whose center points have thermal inertias greater than 500 J m^{-2} K^{-1} $s^{-0.5}$ (PSP_007445_2035 and PSP_007735_2030, but not PSP_007154_1915), have obvious bedrock exposures, indicating that the fine component inertia is lower.

3.4.3. GRS signatures

Analysis of elemental mass fractions in the upper ~ 50 cm derived from the Gamma Ray Spectrometer (GRS) investigation indicates that most of Tharsis is within an area relatively rich in chlorine and depleted in silicon and iron (Karunatillake et al., 2009). Together with the HiRISE images indicating a mantle at least 4 m thick (Keszthelyi et al., 2008), this points to more than a significant coating of dust. The GRS data are best matched to a MER-like dust composition with added salts and are poorly correlated to results expected from coarse soils (sulfur abundance, expected to correlate with that of chlorine, was not reduced in the Karunatillake et al. study). Although these data have 300 km spatial resolution, they show a distinct regional difference compared to that expected for basaltic rock or sand that forms bedforms elsewhere on Mars.

3.4.4. Dark collar

Images within the region demarcated by the seasonal dark collar on Olympus Mons show yardangs and wind tails. Ridges are seen in some images, but are completely lacking in others. No images show a surface covered in ridges, in contrast to many areas outside of the collar. Regional-scale atmospheric models show some of the highest winds on the upper flanks (Kahre et al., 2006; Michaels et al., 2006), near the location of the collar, with near-surface speeds up to 100 m s^{-1}. HiRISE acquired an image of the collar boundary on Pavonis Mons (Fig. 7f). At a coarse scale

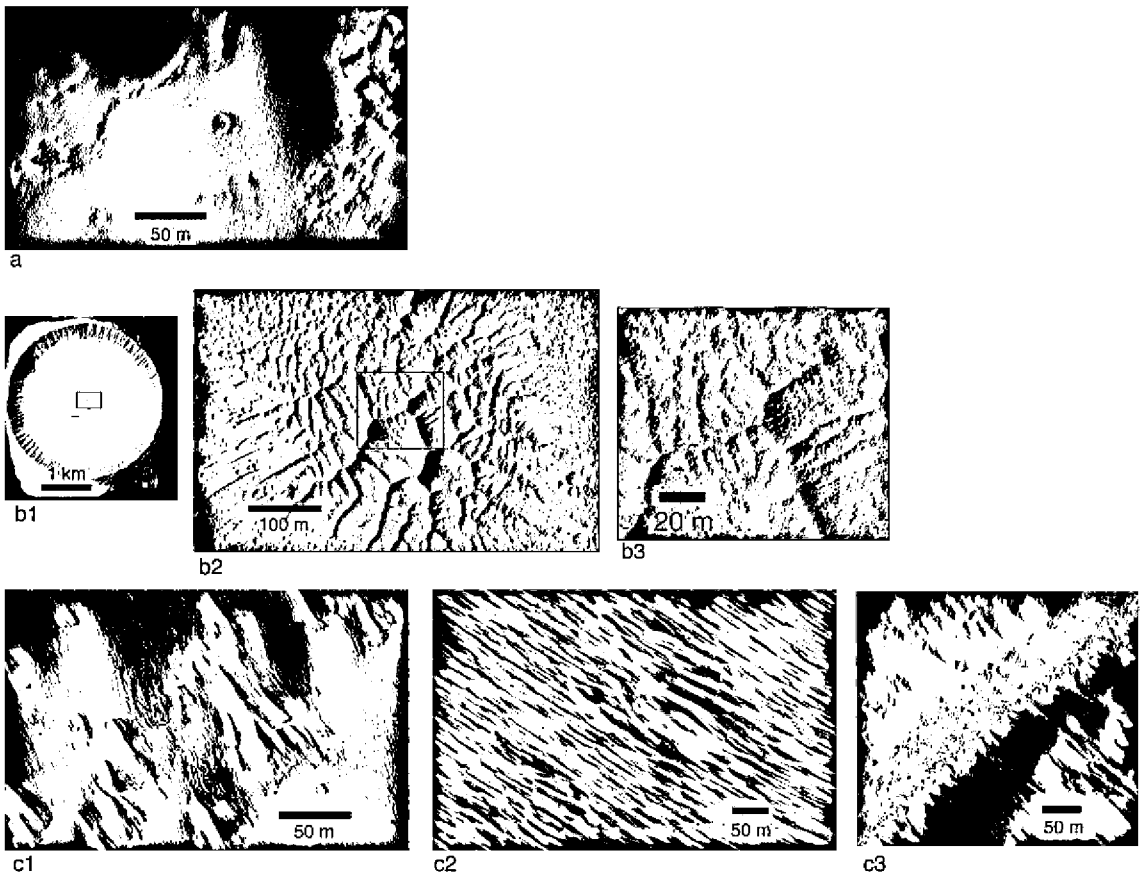

Fig. 6. Some examples of reticulate textures on and near Ascraeus Mons. (a) Honeycomb textures on various surfaces on the plains southeast of Ascraeus. Fuzzy areas all occur to the northeast of topographic elevations (PSP_002209_1865). (b) Honeycomb forms overlying dunes in a crater, on plains southeast of Ascraeus (PSP_007892_1865). (c) Yardangs and indurated surfaces with superposed dark ridges, interpreted as small linear bedforms. (c1) PSP_010081_1875; (c2) PSP_003686_1865; (c3) PSP_001985_1860.

of a few meters, linear ridges are apparent on both surfaces. However, at the limit of HiRISE resolution, the finest scale ridges are absent within the dark region. The dark collar also has a scalloped texture in many places.

3.4.5. "Fuzzy" terrain

Many reticulate ridges are located within regions that appear blurred. This is particularly obvious in several images on the plains west of the Arsia flanks (Fig. 13b and c), in locations on the SE Arsia flank (Fig. 13f), and south of Ascraeus (Fig. 6a and c2). Such terrain was noted in coarser-scale MOC images of the north flank of Ascraeus Mons and attributed to "highly modified surface features" (Malin and Edgett, 2001). Over wide areas this is also seen in some of the HiRISE images (Figs. 6c2, 13b, and c). This "fuzziness" is also present more locally. For example, the fuzziness in Fig. 6a occurs exclusively northeast of topographic obstacles and the streaks of "fuzziness" in Fig. 13f are confined to the northern part of the crater.

3.5. Yardangs, indurated surfaces, and some relationships to reticulate ridges

Yardangs cover many areas on and near the volcanoes (Figs. 11 and 14). In addition there are relatively flat areas containing scallops that lack the topography consistent with yardangs. These are interpreted as wind-scoured indurated surfaces. These are common on the mid-lower flanks of Olympus Mons, the plains south of Olympus, plains west and south of Ascraeus Mons (Fig. 6c2), on the plains southeast of Pavonis Mons (Fig. 7e), and in some areas on and near Arsia Mons (Fig. 13e). In some cases, linear reticulate ridges superpose the scalloped surfaces and are oriented perpendicular to the long axes of the scallops (i.e., parallel to the short axes). This is seen in high concentration (Fig. 7a) or areally of lower density as light-dark bands (Fig. 6c). Some craters within these scalloped areas lack raised rims and do not appear to have disrupted the nearby ridges (Fig. 7d and e). In some areas, it appears that the indurated surface is itself composed of reticulate ridges that have been partially stripped away (Fig. 13e). There are no obvious albedo and thermal inertia differences for images in which yardangs/indurated surfaces or reticulate bedforms predominate or are mixed together (Fig. 12).

4. Discussion

4.1. The nature of reticulate ridge material

There are several salient findings as just described that constrain models on the nature, origin, and evolution of the reticulate ridges.

(1) The orientation of linear and accordion ridges is consistent with aeolian saltation. Linear and 1st order ridges of accordions on the volcano flanks are oriented circumferentially around the flanks. This orientation, combined with those of yardangs and wind tails perpendicular to the ridges, is indicative of downslope winds and is supported by previous observations of the orientation of wind streaks on the margins of the dark collars and predictions of regional atmospheric models.

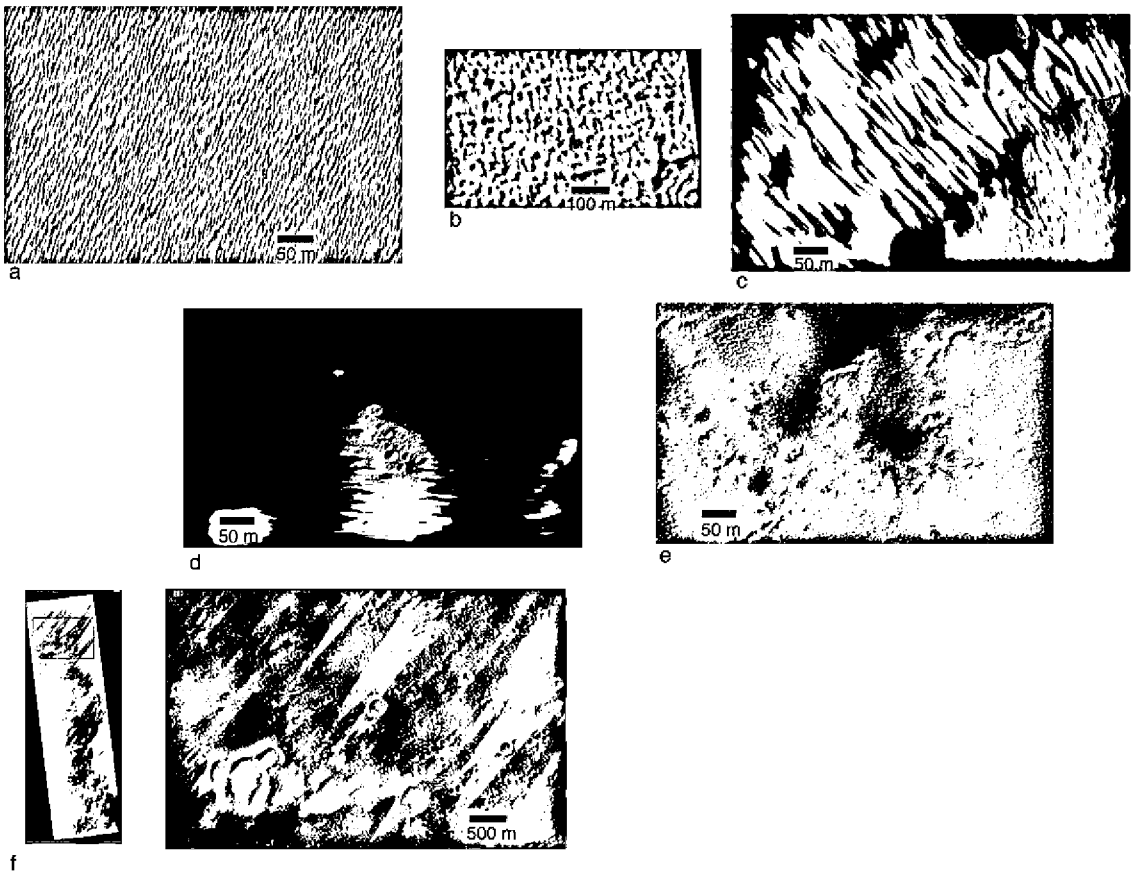

Fig. 7. Some examples of reticulate textures on and near Pavonis Mons. (a) Linear bedforms overlying a sculpted texture (PSP_008143_1835). (b) Light-dark bands (interpreted as bedforms) overlying the northern slopes of some sculpted textures (PSP_009712_1785). (c) Dark bands overlying sculpted terrain northeast of a pit. Note slope streak scars in pit and alcoves in pit edge that are aligned with the bands, indicating a common wind direction responsible for both features (PSP_010213_1785). (d) Fresh crater cluster superposing linear reticulate ridges. The ridges are not disrupted, indicating that migration has not occurred since impact, suggestion induration (PSP_009079_1810). (e) Another fresh crater cluster on the plains southeast of Pavonis Mons. The honeycomb ridges are not disrupted by the craters, indicating an indurated surface (PSP_010292_1785). (f) Margin of Pavonis Mons dark collar showing streaks from slope winds (PSP_009646_1795).

(2) In contrast, the interior of calderas and other depressions are almost exclusively covered with honeycombs rather than linear and accordion forms. It is within these regions where enhanced turbulence and flow reversals induced by the confining walls are expected (Rafkin et al., 2001), and bedforms with multiple orientations (such as occurs at coarser-scales in craters, such as Victoria) result.

(3) The low abundance of fine-scale ridges within the dark collars (e.g., Fig. 7f) is indicative of high winds sweeping away particulate material with sufficient speeds to cause suspension. In contrast, the presence of more reticulate bedforms outside the collars suggests lower speed winds capable of saltation instead of suspension.

(4) The concentration of reticulate bedforms is consistent with an airfall source influenced by near-surface winds. For example, bedforms are abundant within deep, closed depressions, such as the calderas, where the airfall material should accumulate over time. In contrast, the abundance of reticulate bedforms on the flanks near the calderas is low, with occurrences there most common adjacent to downslope topographic obstacles such as crater walls (Fig. 10). Reticulate ridges are much more common on the lower flanks. These observations are consistent with a net downslope transport of material by slope winds.

(5) The reticulate bedforms and yardangs have high albedos and low thermal inertias (Fig. 12), consistent with a dusty, low density material or with a surface covered by dust and not by dark, basaltic sand. Large seasonal variability and diurnal differences of the apparent thermal inertia indicates that the Tharsis Montes have a heterogeneous surface (Putzig and Mellon, 2007a), possibly attributable to a combination of layering, horizontal mixtures, and sub-pixel slope effects (Putzig and Mellon, 2007b). Any layering could result from induration into more cohesive yardang/duststone material. There is no obvious difference in thermal inertia of images dominated by reticulate ridges versus those containing mostly yardangs. This is probably because the yardangs are covered with dust, masking a higher thermal inertia expected for a more indurated surface. More detailed studies of thermal data for this region, as well as laboratory investigations of dust aggregates, are needed.

(6) The reticulate bedforms and yardangs overlap GRS signatures rich in Cl and poor in Si and Fe, indicating a composition of dust with added salts to depths of ~50 cm (Karunatillake et al., 2009). Cohesive soils on Mars are rich in sulfur and chlorine (Clark et al., 1982; Rieder et al., 2004). Therefore, the GRS results are consistent with some form of salt-rich, possibly cohesive, dust, not basaltic sand.

4.2. Constraints on reticulate materials from aeolian physics

The co-location of reticulate bedforms in regions of low thermal inertia, high albedo, high dust index (Ruff and Christensen, 2002),

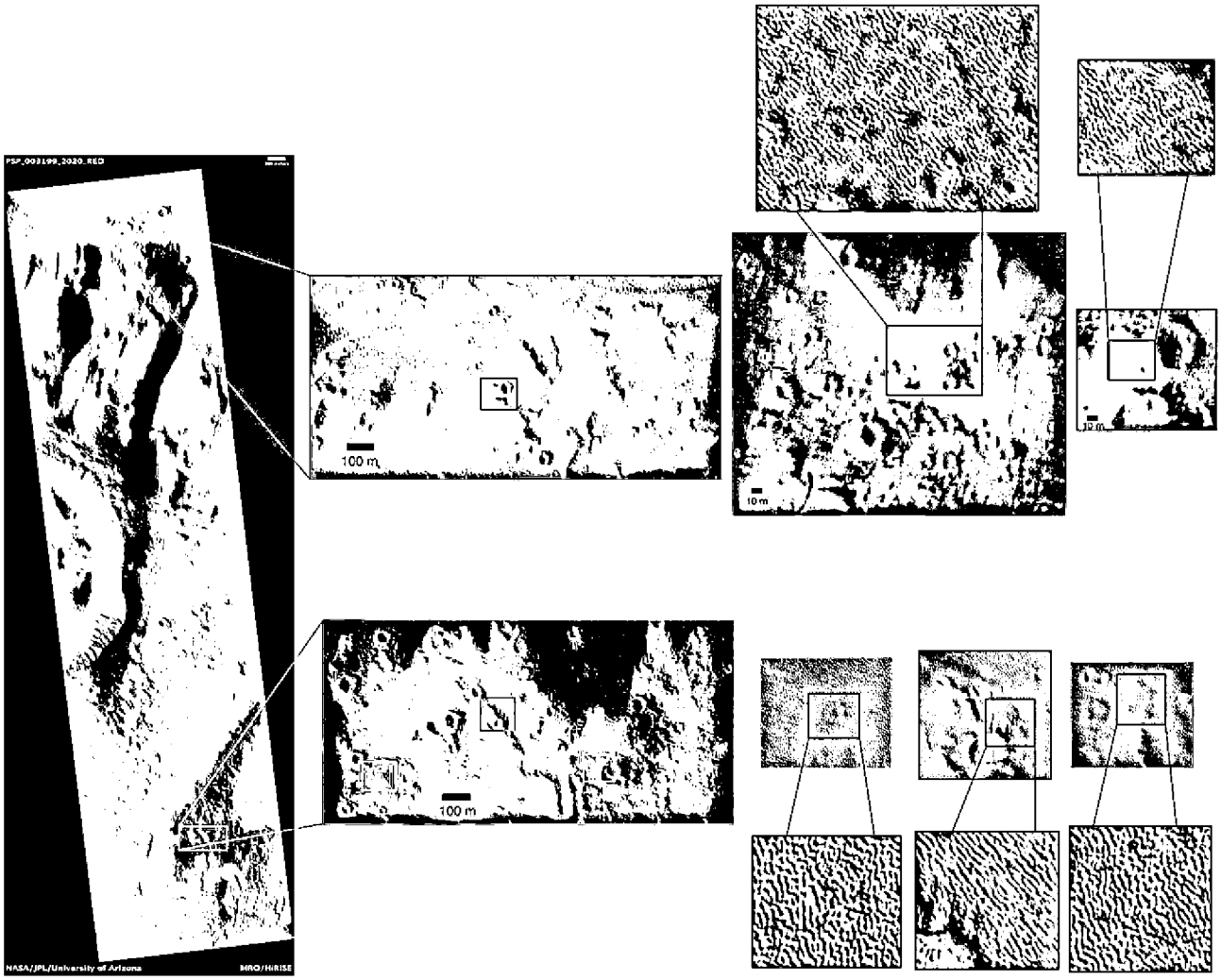

Fig. 8. Example of linear bedforms on the volcano flanks. This example is on the northeast edge of the flank of Olympus Mons. Colored boxes show location of enlargements to the right. Black boxes within those show outline of 2×, stretched enlargements above and below (PSP_003199_2020). (For interpretation of the references to color in this figure legend, the reader is referred to the web version of this paper.)

and seasonal dust transport mechanisms indicates that at least the upper few centimeters cannot be made of sand or granules that compose other dunes and ripples on Mars. The GRS data, with a detection depth of ~50 cm, and the lack of sand sources or effective transport mechanisms, strongly suggests that the entire mantle is mostly or completely composed of dust or some dust-like material (see Section 4.6.1 for additional discussion). The location of the reticulate bedforms at the highest elevations of Tharsis indicates that saltation occurs at very low atmospheric densities even though suspension is also active, as evidenced by the dark collars and possible dust streaks seen in some HiRISE images (Fig. 6a and maybe Fig. 13d).

The particle size and density of the reticulate bedform grains can be constrained by consideration of the threshold curve and the saltation/suspension boundary (Fig. 15). The former defines the friction speed (u^*) as a function of particle size needed to initiate particle motion. Numerous experimental and theoretical investigations show that the shape of the curve is concave, with a minimum near a few hundred microns or less (Bagnold, 1941; Greeley and Iversen, 1985; Shao and Lu, 2000). The upward slope for larger grain sizes is due to the greater shear stress needed to lift heavier grains. At smaller grain sizes, particle cohesion and low Reynolds number effects that inhibit interaction of the wind with the surface (due to small grains being immersed in the laminar sub-layer), result in an inverse correlation between shear stress and particle size. Friction speed is proportional to the square root of particle weight divided by atmospheric density. Therefore, friction speeds needed to liberate equivalent density particles on Mars, with a gravity of ~0.4 and atmospheric density ~0.01 that of terrestrial values, are about 5–9× greater than on Earth. Wind speeds near the surface (V_∞) are about 15–50× the friction speed depending on the surface roughness at scales of ~0.1– 10 s of centimeters (Greeley et al., 1980).

It is very common in the literature to describe the threshold curve as the boundary between a stable surface and saltation. However, this description is only applicable for the portion of the curve above which grains will not be suspended. The boundary between suspension and saltation is centered on where the terminal fall velocity balances the friction speed, which is of the same magnitude as the vertical component of turbulence (Greeley and Iversen, 1985). Superposing threshold and saltation/suspension boundary curves illustrates the theoretical behavior of particles as a function of friction speed and size. Here, we compute threshold friction velocity (u^*_t) based on the derivation of Shao and Lu (2000):

$$u_{*t} = \left(0.0123\left[\sigma_p g d + \frac{\gamma}{\rho d}\right]\right)^{0.5} \quad (1)$$

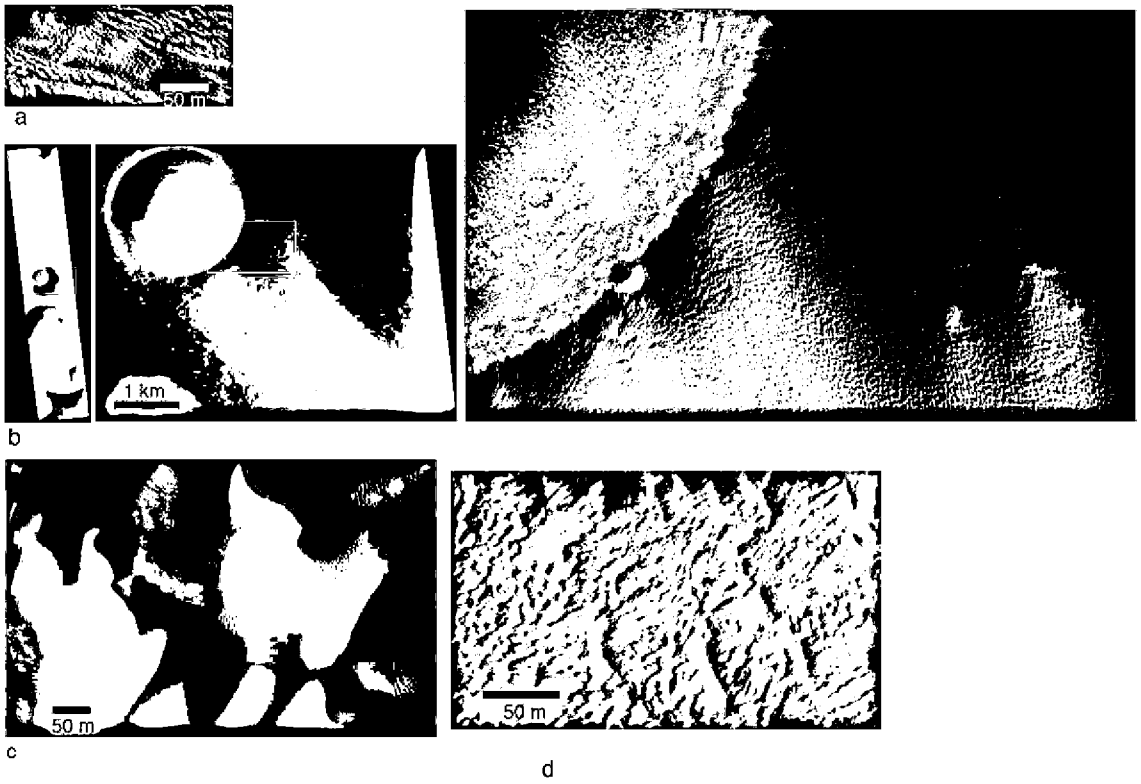

Fig. 9. Examples of reticulate bedforms outside of the volcanic regions. (a) Basal unit in Chasma Boreale (PSP_009914_2750). (b) Crater wind streak in Syria Planum (PSP_009039_1660). (c) On the surface of dunes in Lyot Crater (PSP_009179_2305). (d) Mound within a crater east of Schiaparelli (PSP_010419_1770).

where σ_p is the particle density (ρ_p) divided by the atmospheric density (ρ), g is the acceleration of gravity, d is the particle diameter, and γ an empirical coefficient equal to $\sim 3 \times 10^{-4}$ kg s^{-2}. This is a theoretical expression that agrees closely with wind tunnel measurements under a variety of conditions (Greeley and Iversen, 1985). Terminal fall velocity (u_f) is taken from the standard equation

$$u_f = \frac{gd^2}{18\mu}\left(\rho_p - \rho\right) \tag{2}$$

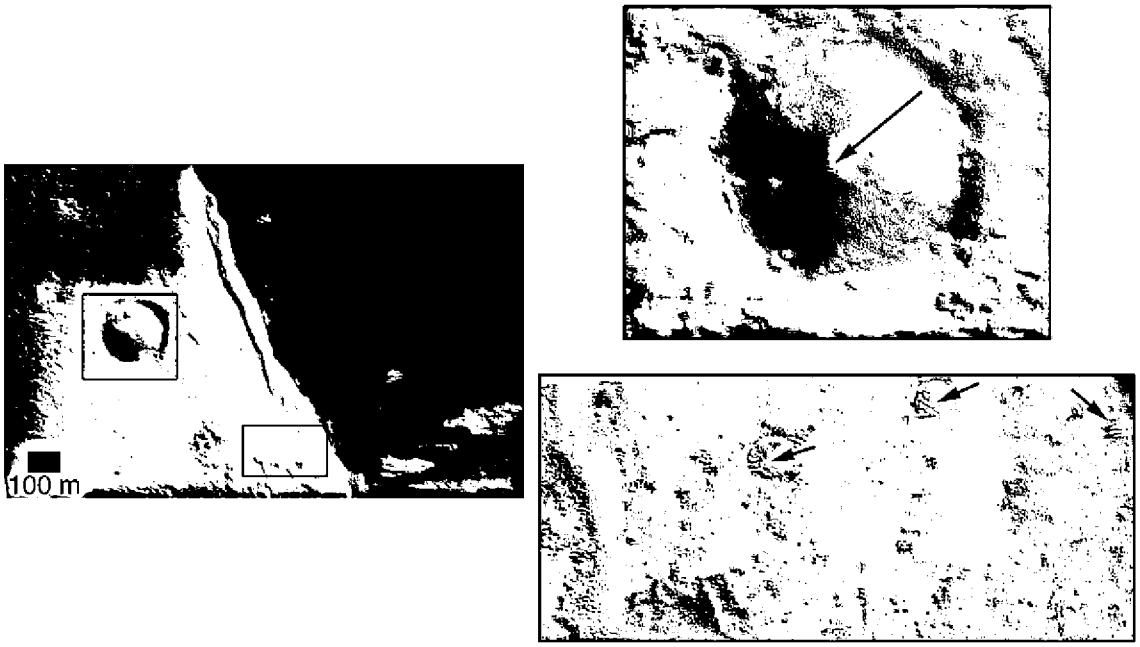

Fig. 10. HiRISE image PSP_004821_1985 showing the western edge of the Olympus Mons caldera. Colored boxes show location of enlargements to the right. Reticulate bedforms are clustered on the side of craters opposite the caldera (bedforms shown by arrows), consistent with airfall deposition and downslope transport by near-surface winds. (For interpretation of the references to color in this figure legend, the reader is referred to the web version of this paper.)

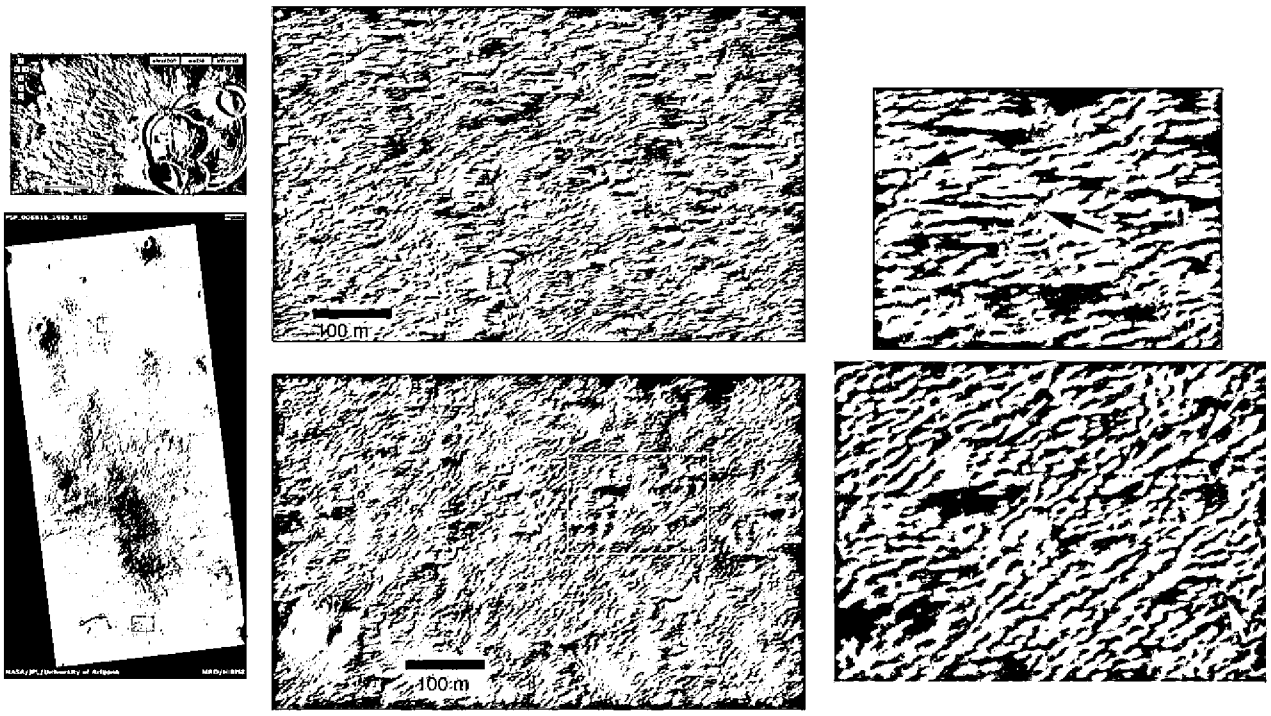

Fig. 11. Details of yardangs on the western flank of Olympus Mons in HiRISE image PSP_008816_1985. Note the blunt to tapered edge of most yardangs and the wind tails in the lee of rocks, going from right to left, consistent with downslope winds. Black arrows in the upper right sub-frame show rocks to the west of which are linear ridges interpreted as wind tails. The white arrows in the lower right sub-frame show yardangs. Upper left framelet shows the location of the HiRISE footprint, at lower left. Colored boxes show location of enlargements to the right. (For interpretation of the references to color in this figure legend, the reader is referred to the web version of this paper.)

where μ is the dynamic viscosity. Values used to generate the curves and lines in Fig. 15 are given in Table 1.

Four zones can be defined when the functions described by Eqs. (1) and (2) are superposed. Friction speeds just above threshold, grains will go either into suspension or saltation depending on their particle size. If friction speed increases significantly above threshold, the size of particle that can remain suspended increases. When u^* is below threshold, no particles are liberated from the surface. Particle sizes to the left of the saltation/suspension boundary will accumulate on the surface as airfall. Those to the right of the curve consist of grain sizes that are generally too coarse to get suspended, such that at low friction speeds there is no airfall accumulation and the surface can be considered stable.

We now consider the conditions for the reticulate bedforms. Fig. 15a and b compare quartz particles at STP on Earth and basalt grains at standard conditions on Mars, as defined in Table 1. As described above, friction speeds (and therefore near-surface winds) needed to move material off a surface are about 6–9× greater for the martian case at a pressure of 6.1 mb (not quite 5–9× as described above because we are using two different particle densities, quartz (Earth) and basalt (Mars)). Moving to the extreme case at the top of the volcanoes, where pressure can be 0.5 mb or less, friction speeds at threshold are about another 3.5× greater than at 6.1 mb on Mars and ~20–30× greater than quartz on Earth (Fig. 15c). However, plotting basalt is not applicable for dust. *In situ* and spectroscopic measurements of martian dust indicate a basaltic composition, with a thin coating of ferric oxides (Morris et al., 2000; Goetz et al., 2005), consistent with altered (not primary) basalt. An analog material is JSC-Mars 1, a volcanic tephra from Hawaii, with a particle density of 1910 kg m^{-3} and a bulk density of 870 kg m^{-3} (Allen et al., 1998). The latter is used here because this density is more appropriate to aggregates. Because both of these densities are less than that of basalt, the threshold curve is lowered and the saltation/suspension boundary moves to the right (Fig. 15d).

These curves constrain the friction speeds and particle sizes of the reticulate materials, which can then be compared to atmospheric wind models, thermal inertia measurements, and other data on martian dust. Because the bedforms exist at the highest elevations, these highest friction speeds (because of the low atmospheric density) provide an upper bound for computation. Values are at least 5 m s^{-1}, increasing to >10 m s^{-1} for particles 10 μm in diameter and smaller, which translates into near-surface wind speeds of ~75 m s^{-1} or greater, depending on surface roughness. Based on modeling on the Tharsis volcanoes, velocities on the caldera rims and flanks can be as great as ~60 and 100 m s^{-1}, respectively (Michaels et al., 2006). At lower elevations, correspondingly lower friction speeds are required.

However, the saltation/suspension boundary curve clearly shows that particles less than a few hundred microns in size will be suspended once liberated from the surface at all elevations on the volcanoes. They will not saltate and make bedforms. Therefore, we propose that dust aggregates, not micron-scale dust that is suspended in the atmosphere, makes up the reticulate bedforms. This conclusion is not necessarily in conflict with the low thermal inertia measurements, as aggregates are effectively small particles loosely bonded together that may retain the thermal properties of smaller, un-aggregated particles. Furthermore, thermal inertia is proportional to the square root of the product of thermal conductivity, density, and specific heat ($I \propto (\kappa\rho C)^{0.5}$). Although conductivity is inversely proportional to particle size at martian pressures, with the thermal conductivity of 10 μm grains relative to 100 μm lower by a factor of 3–4 (Presley and Christensen, 1997a,b), the bulk density of JSC-Mars 1, at 870 kg m^{-3} (Allen et al., 1998), is 3.5× less than that of basalt, thereby counteracting the thermal conductivity effect. Additionally, the relationship between thermal inertia and particle size at low pressures and high elevations is complex, leaving some ambiguity in a unique interpretation (Bridges, 1994). Finally, small

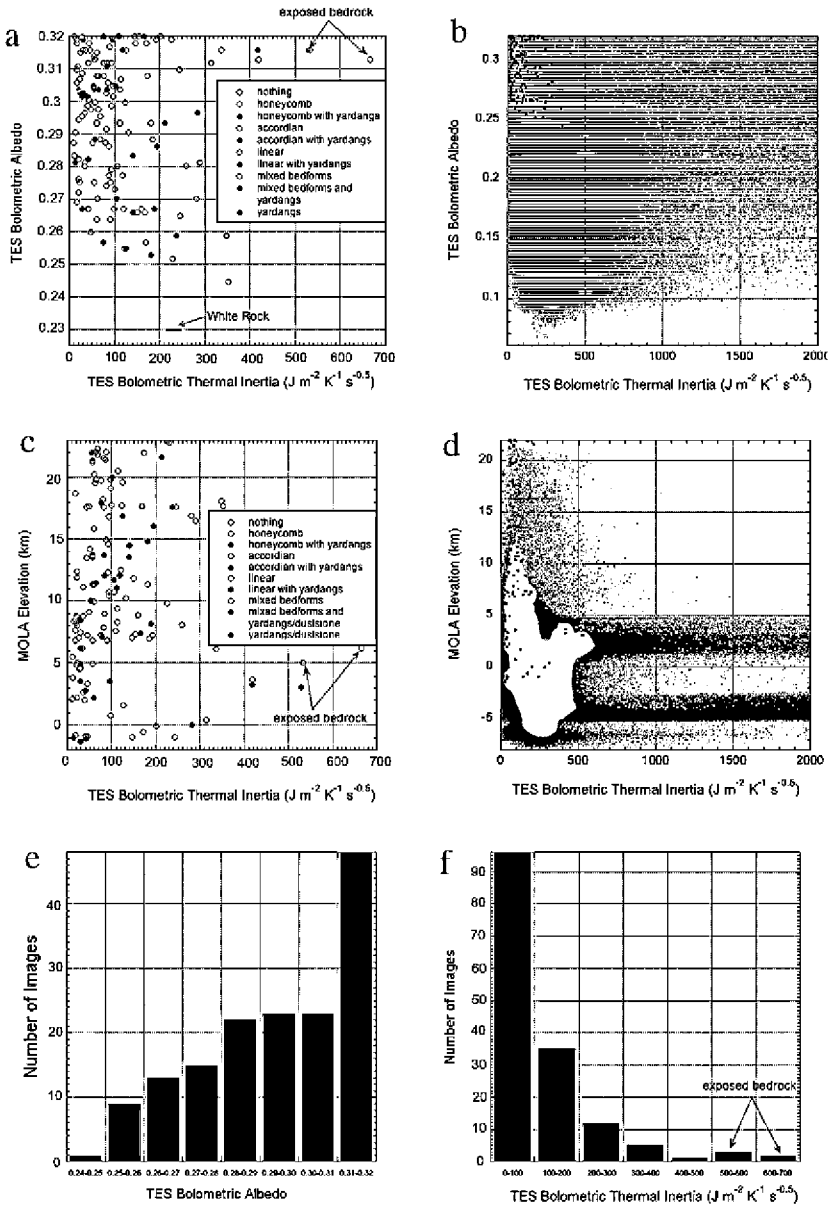

Fig. 12. Thermal inertia, albedo, and elevation of the center points of the HiRISE images used in this study and comparisons to the global distribution. See text for details on the data. (a) Albedo versus thermal inertia for all images, with White Rock (Ruff et al., 2001) shown for comparison. Locations with high inertia and exposed bedrock are highlighted. (b) Albedo versus inertia corresponding to the HiRISE images (black points) compared to the global distribution (red points). (c) Elevation versus thermal inertia for all images, with those having high inertia and exposed bedrock highlighted. (d) Elevation versus inertia corresponding to the HiRISE images (black points) compared to the global distribution (red points). (e) Histogram of number of HiRISE images in this study whose center points fall within the given albedo bin. (f) Histogram of number of HiRISE images in this study whose center points fall within the given thermal inertia bin. (For interpretation of the references to color in this figure legend, the reader is referred to the web version of this paper.)

size dust from recent airfalls may coat the aggregates, further complicating the signature.

In situ observations of martian dust show that dust aggregates are common on the surface. Microscopic Imager data from the MER *Spirit* rover show dust clumps several hundred microns in diameter (Herkenhoff et al., 2004, 2006, 2008; Sullivan et al., 2008), equivalent to the size proposed here that is needed to participate in saltation. The aggregates are easily crushed (Herkenhoff et al., 2008), indicating a low strength and density. Aggregation of fine particles on Mars to form "cloddy material" has been proposed to occur via electrostatic charging (Shorthill et al., 1976; Greeley, 1979) or from sublimation residues (Storrs et al., 1988). Although none of these observations demonstrate conclusively that aggregates can saltate, there are analogs materials on Earth that form saltation bedforms. Clay aggregates ("parna") derived from dry or ephemeral lake beds form lunettes, low transverse duneforms, such as occur in Australia (Bowler, 1973). Parna sheets have been hypothesized to occur on Mars (Greeley and Williams, 1994), but have not been identified. Aggregates have also been proposed to compose the low thermal inertia dunes and materials in the north polar erg (Herkenhoff and Vasavada, 1999).

4.3. Nature of indurated surfaces and yardangs

The alignment of linear ridges with the short axes of scallops in many light-toned areas is consistent with the scalloped, underlying surface being composed of abradable material that is partially covered with bedforms (Figs. 7a, c and 11c). The alignment of the scallops and putative bedforms is in agreement with a dominant wind regime causing abrasion of a hard surface (i.e., forming the scallop major

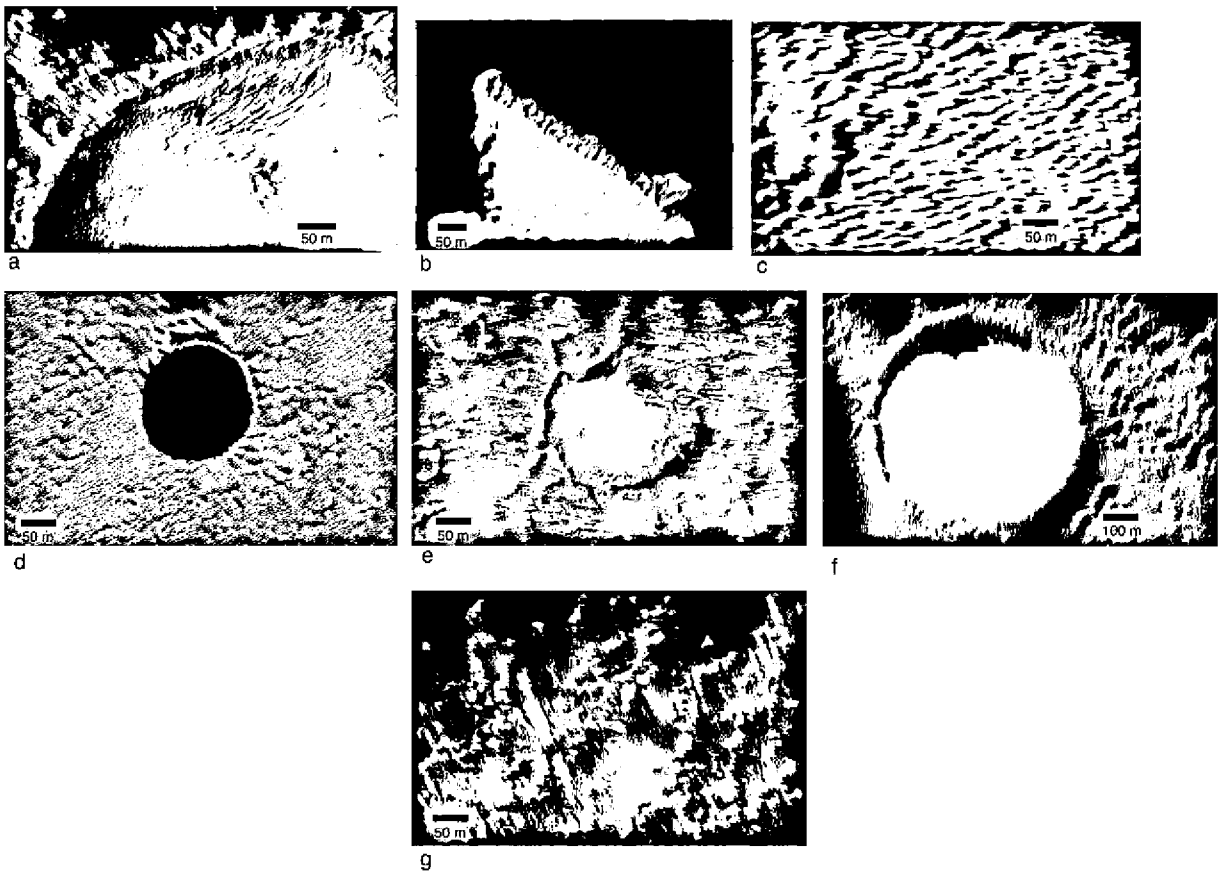

Fig. 13. Some examples of reticulate textures and other features on and near Arsia Mons. (a) Honeycomb textures within pit and linear textures on plains to the north (PSP_007167_1875). (b) A pit chain surrounded by fuzzy terrain (PSP_006680_1740). (c) Another example of fuzzy terrain. In this case, light-dark bands, interpreted as linear bedforms, are seen at overlying the variegated terrain (PSP_009185_1770). (d) Skylight pit surrounded by reticulate ridges. Note that the scale of the honeycomb ridges north of the pit is finer than elsewhere and that this overlaps with dark material, probably blown out of the pit. This is evidence that the honeycombs are bedforms (PSP_004847_1745). (e) Honeycomb hardened mantle that appears stripped off of the northeast edge of crater (PSP_008565_1720). (f) Crater and surrounding terrain with reticulate textures. Note fuzziness in northern part of crater (PSP_008987_1695). (g) Yardang field, identified by blunt-to-tapered (upwind to downwind) morphologies of the high standing topography. Reticulate ridges are seen both in the yardang structure (upwind, bright material) and as superposed bedforms on the downwind edges. This is indicative of active etching of duststone as well as moving bedforms on the surface (PSP_008486_1690).

axes) and saltation of particulate material, respectively. The blunt-to-tapered vector of many yardangs in Tharsis are aligned with the long axes of the scallops. Such a relationship is consistent with wind etching of rock. The presence of fresh craters that lack ridges in their interior and do not disrupt the ridges of the surrounding plains (Fig. 7d) indicates a ridged indurated surface resistant to impact shock and bedform migration. Finally, the indurated surfaces in Tharsis occur within areas of low thermal inertia, which would not be expected if the material is high density bedrock, like basalt.

Similar erosion textures are found on the yardangs that compose White Rock in Pollack Crater. It has a thermal inertia of $232 \pm 14\,J\,m^{-2}\,s^{-0.5}\,K^{-1}$, an albedo of 0.23, and lacks prominent spectral features at near-infrared and thermal wavelengths, consistent with indurated dust (Ruff et al., 2001; Gondet et al., 2006). Its thermal inertia overlaps those of the Tharsis bedforms and yardangs, but its albedo is lower (Fig. 12). The differences in albedos are probably due to the higher apparent surficial dust cover in the Tharsis area as indicated by the TES dust index (Ruff and Christensen, 2002), and not a difference in fundamental physical properties among yardangs.

4.4. Proposed model for the origin and evolution of reticulate bedforms

Our working hypothesis is that many reticulate ridges are saltation bedforms consisting of dust aggregates. We extend this to a proposed sequence of events that explains how these form and can possibly evolve into yardangs. This is considered a working model of which several details are still incompletely understood and should be considered a hypothesis that can be tested by future studies.

Initially, dust is suspended in the martian atmosphere (Fig. 16). It settles in quiescent periods, when the magnitude or duration of surface friction speeds is insufficient to re-suspend more dust than is being deposited from the atmosphere. When friction speeds increase again, the dust is re-suspended. At times when dust is on the surface, it aggregates with nearby settled particles, initially due to electrostatic forces and later possibly from chemical cementation. The aggregation process causes the average particle size to grow. The aggregates become suspended again in high wind events, with some broken back down into smaller particles. However, a certain fraction will continue to grow over time, eventually reaching a size, as seen at the MER landing sites (Herkenhoff et al., 2004, 2006; Sullivan et al., 2008), of a few hundred microns. Subsequent winds above threshold will saltate, rather than suspend, these materials, forming bedforms. Aggregates within calderas and other depressions will be blown about by winds from multiple directions, forming the honeycomb morphology. Aggregates on the flanks will be blown down slope, forming linear and accordion bedforms, and increasing in concentration at lower elevations.

There must be some subtle balance between aggregates that break apart upon collision, and thereby get suspended and re-enter this cycle, versus those that are of sufficient strength to survive col-

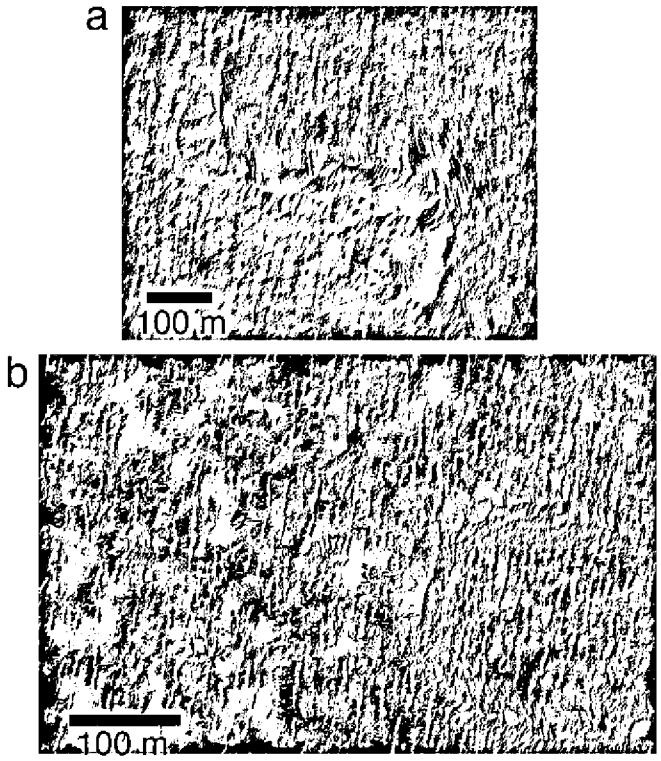

Fig. 14. Examples of yardangs with a reticulate morphology SE of Arsia Mons: (a) PSP_010345_1635, (b) PSP_010345_1635.

lision, form bedforms, and subsequently saltate again. Certainly the aggregates measured by MER were weak (Herkenhoff et al., 2008), but whether all aggregates have similar properties and how this relates to their ability to survive saltation is not known (it is a potential avenue for future experimental work). It is likely that low energy collisions will occur in areas where aggregates are saltating over an underlying bed of other aggregates or fine dust. In these cases, the saltating aggregates are more likely to remain intact. Where the underlying surface is indurated, saltating aggregates have a greater chance of being destroyed. Therefore, the induration process not only removes aggregates from the system by binding them to the surface, but may also act as agents of aggregate attrition, such that only the hardest, most well bound aggregates survive.

4.5. Model for the formation of yardangs from dust aggregates

As evident in HiRISE images of Tharsis, yardangs and presumed indurated surfaces are intermixed with the reticulate bedforms. As a more speculative extension of our model for dust aggregates, we consider how the yardangs and indurated surfaces could be related. Under this hypothesis, some aggregates will continue to grow, such that they again fall below the threshold curve. This may initially occur via electrostatic charging, but, over time, cohesion could increase due to natural geochemical processes on Mars, such as cementation by sulfur- and chlorine-rich salts, as indicated by the high S and Cl contents of cohesive and hardened soils on the planet (Clark et al., 1982; Rieder et al., 1997, 2004). Cl and S may be mobilized by diffusion of water vapor through the soil, a process that can occur even in the equatorial regions (Jakosky and Christensen, 1986). Other possible mechanisms include degassing, fluid mixing, cooling, and evaporation (Pain et al., 2007). However, the details of how these processes would occur for dust aggregates are not well understood, as *in situ* measurements of this terrain have not been made by any Mars mission, although Pathfinder and MER provided some data on dust and dust aggregate properties. Regardless of how this process occurs, we propose that subsequent wind abrasion sculpts the now hardened soil into the classic yardang forms observed. Because of the probable limited sand supply on the volcanoes (see below), it seems that the yardangs must be abraded by dust aggregates or deflated by the wind, implying that they are rather weak. The best terrestrial physical analog are yardangs made from poorly indurated lake sediments that appear to erode predominantly from wind deflation (McCauley et al., 1977), requiring no supply of sand that is otherwise needed to abrade harder materials such as rocks (Laity and Bridges, 2009). This process of yardang erosion may also liberate particles that can be re-suspended. Such "duststone" may be a common rock on the martian surface and serve as both a sink and possible source for dust.

4.6. Alternate hypotheses

Although we favor a dust aggregate explanation for the reticulate bedforms, there are other hypotheses for the material composition and morphology worthy of consideration.

4.6.1. Material composition

The reticulate bedform texture is similar to that documented for sand bedforms on Earth and elsewhere on Mars (although the scale of the reticulate forms seems finer; a quantitative comparison has not been done). Indeed, it is this similarity in morphology that leads us to our hypothesis that these are saltation features. However, despite the common textures, it is unlikely that the reticulate bedforms are composed of traditional sand or sand covered by dust (by "traditional," we mean particulate material produced from the weathering of primary rock, such as dune and beach sand on Earth). Although a dust cover could produce the observed low thermal inertia, high albedo, and dust-like GRS signatures, there are several arguments against significant volumes of sand existing on the volcanoes: (1) The mantle that covers the Tharsis Montes is at least 4 m thick and, even in cross-section, exhibits a light tone similar to dust (Keszthelyi et al., 2008), consistent with the high albedo and low thermal inertia seen at coarser-scale by orbital instruments. These observations indicate thick accumulations of a material that closely matches its surface properties. Similarly, GRS data are consistent with thick dust accumulations in Tharsis (down to the detection depth of about 50 cm) (Karunatillake et al., 2009). (2) A thick mantle precludes any locally-derived sand derived from breakup of the underlying basalt making it to the surface in sufficient quantities. Also, there are few craters that have punched through the mantle and could serve as a local source of impact-derived sand. (3) Significant sand transport from outside of Tharsis is inhibited by the wind regime on the volcanoes. The orientation of windstreaks and windtails (Veverka et al., 1977; Lee et al., 1982), and of yardangs from this study, show that downslope, not upslope, winds most affect the surface. Therefore, it is difficult to envision how large amounts of sand could be blown from the surrounding plains and up the volcano flanks all the way to the calderas.

A more credible alternate hypothesis could be that the reticulate bedforms are composed partially or entirely of volcanic tephra. This is appealing in that (1) the Tharsis Montes could have expelled tephra in volcanic eruptions, (2) tephra (at least on Earth) occurs in a variety of sizes, up to sand-size and larger, (3) many tephra classes, such as ash and reticulite found in basaltic eruptions, have a low density. Sand-sized, low density tephra should behave much like dust aggregates. Although this hypothesis cannot be discounted, we prefer a dust aggregate model given that the Tharsis

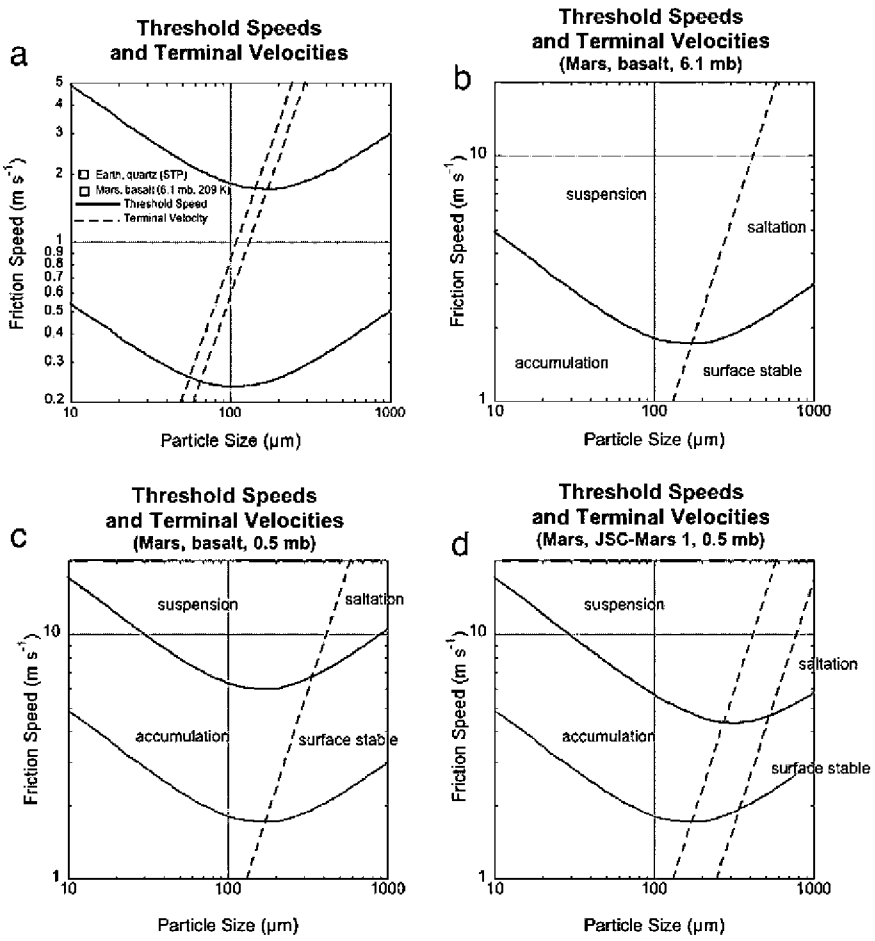

Fig. 15. Superposed curves for threshold friction speed (solid curve) and terminal velocity (dashed line) for various aeolian regimes (Earth = blue, Mars = red). The threshold curve defines the lowest friction speed at which particle motion is initiated. The terminal velocity line defines the boundary between particles that can be suspended and saltated. The two curves define four zones of particle behavior, as discussed in the text. The list of values used to generate the curves is given in Table 1. (a) Comparison between quartz on Earth and basalt on Mars at 6.1 mb. The two grain compositions are used because these constitute the primary mineralogy of sand on the two planets. (b) Close-up of the region for the Mars 6.1 mb basalt curves. (c) Curves for basalt particles at 0.5 mb, shown in red, that is appropriate for the highest elevations of Tharsis. The 6.1 mb curve is shown in gray. (d) Curves for JSC-Mars 1 at 0.5 mb in red, with 6.1 mb curves for basalt in gray. (For interpretation of the references to color in this figure legend, the reader is referred to the web version of this paper.)

Montes are active dust sinks, dust aggregates are verified at the MER sites, and GRS data indicate a dust-like composition.

4.6.2. Morphology

Based strictly on morphology, the honeycomb ridges share some characteristics with landforms that form by mechanisms besides saltation. For example, polygonal cracks of varying scale on Mars have been attributed to seasonally-induced tensile stresses in permafrost (Mellon, 1997; Mellon et al., 2008), desiccation (Lucchitta et al., 1986; McGill and Hills, 1992), and lava cooling (McGill and Hills, 1992). There are various mechanisms to fill such cracks, such as ice or sand wedging in the permafrost case, that can produce polygonal ridges, with the finest scale examples being of similar size to the honeycomb ridges. However, the geologic provenance of the honeycomb ridges precludes a permafrost or desiccation origin and all of these models fail to account for the presence of linear and accordion ridges. Finally, the low thermal inertia, high albedo, GRS dust composition, and the presence of a mantle cover at least 4 m thick indicates material properties distinct from the underlying basaltic lava flows and other sub-strata.

5. Conclusions

Based on observations from numerous HiRISE images and incorporation of other data sets and models, we propose that reticulate bedforms are composed of aggregated airfall dust. This conclusion

Table 1
Parameter values for calculations of particle threshold and terminal velocity.

Parameter	Symbol	Units	Earth	Mars
Particle density	ρ_p	kg m^{-3}	2650 (quartz)	3000 (basalt) 870 (JSC-Mars 1, bulk)
Atmospheric density	ρ	kg m^{-3}	1.28 (STP)	1.54×10^{-2} (6.1 mb, 209 K) 1.27×10^{-3} (0.5 mb, 209 K)
Gravity	g	m s^{-2}	9.81	3.69
Dynamic viscosity	μ	kg m^{-1} s^{-1}	1.74×10^{-5} (STP)	1.06×10^{-5} (209 K)

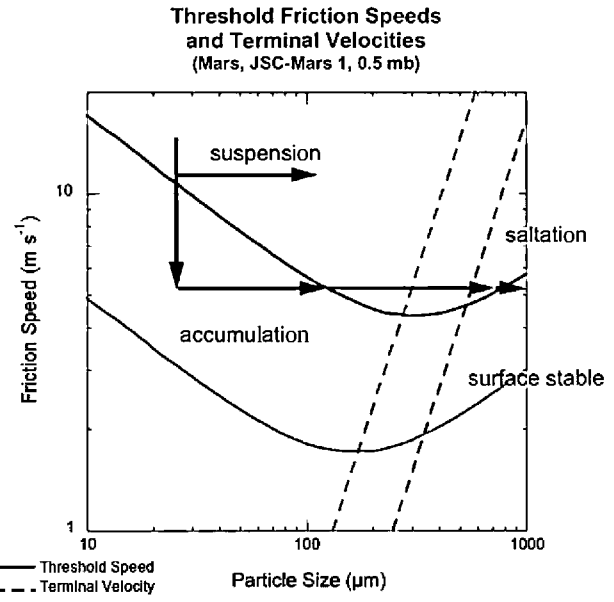

Fig. 16. Schematic diagram of the proposed sequence of events for dust evolution discussed in the text. Red curves show JSC-Mars 1 at 0.5 mb and gray curve is basalt at 6.1 mb. (1) Dust stays suspended in the atmosphere, falling to the surface in quiescent periods when friction speed drop below threshold (orange arrow) (note, most atmospheric dust is on the order of 1–2 μm in size, but is shown here at a larger size to reduce the extent of the *x*-axis). (2) Dust on the surface or in the atmosphere clumps into aggregates (blue arrows). (3) The dust grows in size until it is above the threshold curve and can be re-suspended. (4) Eventually the aggregates reach sufficient size that they are too heavy to get suspended (so below the terminal velocity line), yet above the threshold curve. These particles, shown by the green arrow, will undergo saltation. (5) Further aggregation will again put the particle below the threshold curve, such that they remain stable (purple arrow). Lithification processes allow the aggregate bedforms to harden into yardang "duststone." (For interpretation of the references to color in this figure legend, the reader is referred to the web version of this paper.)

is based on two fundamental sets of observations: (1) The presence in HiRISE images of Tharsis of a mantle at least 4 m thick, the implications from GRS data, the thermal inertia and albedo of the region, and dust transport patterns on Mars all indicate thick accumulations of dust or dust-like material. There is no evidence for significant deposits of traditional sand. (2) The HiRISE images show abundant bedforms whose characteristics are indicative of saltation. We propose that initially micron-scale dust grows over time through aggregation. Once the particle size becomes too large for suspension, the material is transported via saltation when wind speeds are above threshold. Further aggregation effectively stabilizes the particles from further wind transport, allowing them to cohere into soft indurated material that can subsequently be eroded into yardangs.

There are several observations that cannot as yet be reconciled with our simple model. For example, some honeycomb bedforms are found outside closed basins, including some within crater wind streaks. It is possible that complex winds in these locations form the honeycombs. Reticulate ridges in other regions of the planet, such as the north polar layered deposits and near Vallis Marineris, are, at present, not well studied. If they are dust-rich bedforms, why they occur in these particular locations and not elsewhere is a question worthy of further investigation. The fine scale of reticulate bedforms is not understood. Perhaps very small saltation path lengths result from the low density of the aggregates, but further modeling is needed to bolster this hypothesis. More unambiguous results may have to await surface field work and sampling in the Tharsis region.

The results of this paper are therefore most applicable to reticulate bedforms on the low thermal inertia mantle on and near the Tharsis volcanoes. The proposed model offers an explanation for the reticulate ridges that is consistent with a number of data sets. This suggests that dust aggregates are a common saltation bedform in the Tharsis region, and perhaps elsewhere, on Mars.

Acknowledgments

This research was supported by a grant from the MRO Participating Scientist Program. Emily Gorbaty, an intern from Stanford University, measured the dimensions of many reticulate ridges and made Fig. 3. Discussions with S. Karunatillake improved our understanding of GRS measurements of the Tharsis region. The comments of two anonymous reviewers are gratefully acknowledged. The research described in this paper was carried out at the Jet Propulsion Laboratory, California Institute of Technology, under a contract with the National Aeronautics and Space Administration.

References

Allen, C.C., Morris, R.V., Jager, K.M., Golden, D.C., Lindstrom, D.J., Lindstrom, M.M., Lockwood, J.P., 1998. Martian regolith simulant JSC Mars-1. Lunar Planet. Sci. XXIX, Abstract 1690.

Bagnold, R.A., 1941. The Physics of Blown Sand and Desert Dunes. Methuen, London. 265pp.

Beyer, R.A., Hancher, M.D., Broxton, M., Weiss-Malik, M., Gorelick, N., Heldmann, J., Steber, N., Kofman, R., 2007. Google Moon, Google Mars, and beyond. Eos Trans. AGU 88 (52). Fall Meet. Suppl., Abstract P41A-0204.

Bowler, J.M., 1973. Clay dunes: Their occurrence, formation, and environmental significance. Earth Sci. Rev. 9, 315–338.

Bridges, N.T., 1994. Elevation-corrected thermal inertia and derived particle sized on Mars and implications for the Tharsis Montes. Geophys. Res. Lett. 9, 785–788.

Bridges, N.T., Geissler, P.E., McEwen, A.S., Thomson, B.J., Chuang, F.C., Herkenhoff, K.E., Keszthelyi, L.P., Martinez-Alonso, S.E., 2007. Windy Mars: A dynamic planet as seen by the HiRISE Camera. Geophys. Res. Lett. 34. L23205. doi:10.1029/2007GL031445.

Christensen, P.R., 1986. Regional dust history on Mars: Physical properties, age, and history. J. Geophys. Res. 91, 3533–3545.

Christensen, P.R., 1988. Global albedo variations on Mars: Implications for active aeolian transport, deposition, and erosion. J. Geophys. Res. 91, 3533–3545.

Christensen, P.R., and 25 colleagues, 2001. Mars Global Surveyor Thermal Emission Spectrometer experiment: Investigation description and surface science results. J. Geophys. Res. 106, 23,823–23,872.

Clark, B.C., Baird, A.K., Weldon, R.J., Tsusaki, D.M., Schnabel, L., Candelaria, M.P., 1982. Chemical composition of martian fines. J. Geophys. Res. 87, 10,059–10,067.

Edgett, K.S., Malin, M.C., 2000. Eolian bedforms and erosional landforms at high altitudes on the martian Tharsis volcanoes. Lunar Planet. Sci. XXXI, Abstract 1072.

Goetz, W., and 19 colleagues, 2005. Indication of drier periods on Mars from the chemistry and mineralogy of atmospheric dust. Nature 436. doi:10.1038/nature0387.

Gondet, B., Bibring, J.-P., Langevin, Y., Poulet, F., 2006. Composition of White Rock formation within Pollack Crater as inferred from the OMEGA/MEX data. Lunar Planet. Sci. XXXVII, Abstract 1592.

Greeley, R., 1979. Silt-clay aggregates on Mars. J. Geophys. Res. 84, 6248–6284.

Greeley, R., Iversen, J.D., 1985. Wind as a Geological Process. Cambridge University Press. 333pp.

Greeley, R., Williams, S.H., 1994. Dust deposits on Mars – The parna analog. Icarus 110, 165–177.

Greeley, R., Leach, R.N., White, B.R., Iverson, J.D., Pollack, J.B., 1980. Threshold windspeeds for sand on Mars: Wind tunnel simulations. Geophys. Res. Lett. 7, 121–124.

Greeley, R., Lancaster, N., Lee, S., Thomas, P., 1992. Martian aeolian processes, sediment, and features. In: Kieffer, H.H., Jakosky, B.M., Snyder, C.W., Matthews, M.S. (Eds.), Mars. Univ. Ariz. Press, Tucson, pp. 730–766.

Greeley, R., Bridges, N.T., Kuzmin, R.O., Laity, J.E., 2002. Terrestrial analogs to aeolian features seen from the surface of Mars. J. Geophys. Res. 107. 5-1-21.

Hancher, M.D., Beyer, R.A., Broxton, M.J., Kasraie, K., Smith, M.E. 2008. New platforms for web-based lunar and planetary mapping and GIS. Lunar Planet. Sci. XXXIX, Abstract 2263.

Hancher, M.D., Beyer, R., Broxton, M., Gorelick, N., Kolb, E., Weiss-Malik, M., 2009. Visualizing Mars data and imagery with Google Earth. Lunar Planet. Sci. XL, Abstract 2308.

Herkenhoff, K.E., Vasavada, A.R., 1999. Dark material in the polar layered deposits and dunes on Mars. J. Geophys. Res. 104, 16,487–16,500.

Herkenhoff, K.E.and 22 colleagues, 2004. Textures of the soils and rocks at Gusev Crater from Spirit's Microscopic Imager. Science 305, 824–826.

Herkenhoff, K.E., and 41 colleagues, 2006. Overview of Microscopic Imager Investigation during Spirit's first 450 sols in Gusev Crater. J. Geophys. Res. 111. E0S04. doi:10.1029/JE002574.

Herkenhoff, K.E., Golombek, M.P., Guinness, E.A., Johnson, J.B., Kussack, A., Richter, L., Sullivan, R., Gorevan, S., 2008. In-situ observations of the physical properties of the martian surface. In: Bell, J.F., III (Ed.), The Martian Surface: Composition, Mineralogy, and Physical Properties. Cambridge University Press.

Jakosky, B.M., Christensen, P.R., 1986. Global duricrust on Mars: Analysis of remote-sensing data. J. Geophys. Res. 91, 3547–3559.

Kahre, M.A., Murphy, J.R., Haberle, R.M., 2006. Modeling the martian dust cycle and surface dust reservoirs with the NASA Ames general circulation model. J. Geophys. Res. 111. E06008. doi:10.1029/2005JE002588.

Karunatillake, S., Wray, J.J., Squyres, S.W., Taylor, G.J., Gasnailt, O., McLennon, S., Boynton, W., El Maarry, M.R., Dohm, J.M., 2009. Chemically striking martian regions and steal revisited. J. Geophys. Res., in press. doi:10.1029/2008JE003303.

Keszthelyi, L., Jaeger, W., McEwen, A., Tornabene, L., Beyer, R.A., Dundas, C., Milazzo, M., 2008. High Resolution Imaging Science Experiment (HiRISE) images of volcanic terrains from the first 6 months of the Mars Reconnaissance Orbiter primary science phase. J. Geophys. Res. 113. E04005. doi:10.1029/2007JE002968.

Laity, J.E., Bridges, N.T., 2009. Ventifacts on Earth and Mars: Analytical, field, and laboratory studies supporting sand abrasion and windward feature development. Geomorphology 105, 202–217.

Lee, S.W., Thomas, P.C., Veverka, J., 1982. Wind streaks in Tharsis and Elysium: Implications for sediment transport by slope winds. J. Geophys. Res. 87, 10,025–10,041.

Lucchitta, B.K., Ferguson, H.M., Summers, C., 1986. Sedimentary deposits in the northern lowland plains, Mars. Proc. 17th Lunar Planet. Sci. Conf., J. Geophys. Res. 91, E166–E174.

Magalhaes, J., Gierasch, P., 1982. A model of martian slope winds: Implications for eolian transport. J. Geophys. Res. 87, 9975–9984.

Malin, M.C., Edgett, K.S., 2001. Mars Global Surveyor Mars Orbiter Camera: Interplanetary cruise through primary mission. J. Geophys. Res. 106, 23,429–23,570.

McCauley, J.F., Breed, C.S., Grolier, M.J., 1977. Yardangs. In: Doehring, D.O. (Ed.), Geomorphology in Arid Regions. Allen & Unwin, Boston, pp. 233–269.

McEwen, A.S., and 14 colleagues, 2007. Mars Reconnaissance Orbiter's High Resolution Imaging Science Experiment (HiRISE). J. Geophys. Res. 112. E05S02. doi:10.1029/2005JE002605.

McGill, G.E., Hills, L.S., 1992. Origin of giant Martian polygons. J. Geophys. Res. 97, 2633–2647.

Mellon, M.T., 1997. Small-scale polygonal features on Mars: Seasonal thermal contraction cracks in permafrost. J. Geophys. Res. 102, 25,617–25,628.

Mellon, M.T., Jakosky, B.M., Kieffer, H.H., Christensen, P.R., 2000. High-resolution thermal inertia mapping from the Mars Global Surveyor Thermal Emission Spectrometer. Icarus 148, 437–455.

Mellon, M.T., Arvidson, R.E., Marlow, J.M., Phillips, R.J., Asphaug, E., 2008. Periglacial landforms at the Phoenix landing site and the northern plains of Mars. J. Geophys. Res. 113. E00A23. doi:10.1029/2007JE003039.

Michaels, T.I., Colaprete, A., Rafkin, S.C.R., 2006. Significant vertical water transport by mountain-induced circulations on Mars. Geophys. Res. Lett. 33. L16201. doi:10.1029/2006GL026562.

Morris, R.V., and 11 colleagues, 2000. Mineralogy, composition, and alteration of Mars Pathfinder rocks and soils: Evidence from multispectral, elemental, and magnetic data on terrestrial analogue, SNC meteorite, and Pathfinder samples. J. Geophys. Res. 105, 1757–1817.

Pain, C.F., Clarke, J.D.A., Thomas, M., 2007. Inversion relief on Mars. Icarus 190, 478–491.

Presley, M.A., Christensen, P.R., 1997a. Thermal conductivity measurements of particulate materials 1. A review. J. Geophys. Res. 102, 6535–6549.

Presley, M.A., Christensen, P.R., 1997b. Thermal conductivity measurements of particulate materials 2. Results. J. Geophys. Res. 102, 6551–6566.

Putzig, N.E., Mellon, M.T., 2007a. Apparent thermal inertia and the surface heterogeneity of Mars. Icarus 191, 68–94. doi:10.1016/j.icarus.2007.05.013.

Putzig, N.E., Mellon, M.T., 2007b. Thermal behavior of horizontally mixed surfaces on Mars. Icarus 191, 52–67. doi:10.1016/j.icarus.2007.03.022.

Rafkin, S.C.R., Haberle, R.M., Michaels, T.I., 2001. The Mars regional atmospheric modeling system: Model description and selected simulations. Icarus 151, 228–256.

Rieder, R., Economou, T., Wanke, H., Turkevich, A., Crisp, J., Brückner, J., Dreibus, G., McSween, H.Y., 1997. The chemical composition of martian soil and rocks returned by the Mobile Alpha Proton X-ray Spectrometer: Preliminary results from the X-ray mode. Science 278, 1771–1774.

Rieder, R., and 14 colleagues, 2004. Chemistry of rocks and soils at Meridiani Planum from the alpha particle X-ray spectrometer. Science 306, 1746–1749.

Ruff, S.W., Christensen, P.R., 2002. Bright and dark regions on Mars: Particle size and mineralogical characteristics based on Thermal Emission Spectrometer data. J. Geophys. Res. 107 (E12), 5127. doi:10.1029/2001JE001580.

Ruff, S.W., Christensen, P.R., Clark, R.N., Kieffer, H.H., Malin, M.C., Bandfield, J.L., Jakosky, B.M., Lane, M.D., Mellon, M.T., Presley, M.A., 2001. Mars "White Rock" feature lacks evidence of an aqueous origin: Results from Mars Global Surveyor. J. Geophys. Res. 106, 23,921–23,927.

Shao, Y., Lu, H., 2000. A simple expression for wind erosion threshold friction velocity. J. Geophys. Res. 105, 22,437–22,443.

Shorthill, R.W., Hutton, R.E., Moore, H.J., Scott, R.F., Spitzer, C.R., 1976. Physical-properties of martian surface from Viking-1 Lander-Preliminary results. Science 193, 805–809.

Smith, D.E., and 23 colleagues, 2001. Mars Orbiter Laser Altimeter: Experiment summary after the first year of global mapping of Mars. J. Geophys. Res. 106, 23,689–23,722.

Storrs, A.D., Fanale, F.P., Saunders, S., Stevens, J.B., 1988. The formation of Filamentary Sublimate Residue (FSR) from mineral grains. Icarus 76, 493–512.

Sullivan, R., and 10 colleagues, 2008. Wind-driven particle mobility on Mars: Insight from Mars Exploration Rover observations at "El Dorado" and surroundings at Gusev Crater. J. Geophys. Res. 113. E06S07.

Thomas, P., Veverka, J., Lee, S., Bloom, A., 1981. Classification of wind streaks on Mars. Icarus 45, 124–153.

Veverka, J., Thomas, P., Greeley, R., 1977. A study of variable features on Mars during the Viking primary mission. J. Geophys. Res. 82, 4167–4187.

Zimbelman, J.R., Kieffer, H.H., 1979. Thermal mapping of the northern equatorial and temperate latitudes of Mars. J. Geophys. Res. 84, 8239–8251.